2008-01-01

Laboratory Measurements of the Moist Enthalpy Transfer Coefficient

Dahai Jeong
University of Miami, djeong@rsmas.miami.edu

UNIVERSITY OF MIAMI

LABORATORY MEASUREMENTS OF THE MOIST ENTHALPY TRANSFER COEFFICIENT

By

Dahai Jeong

A THESIS

Submitted to the Faculty
of the University of Miami
in partial fulfillment of the requirements for
the degree of Master of Science

Coral Gables, Florida

August 2008

UNIVERSITY OF MIAMI

A thesis submitted in partial fulfillment of
the requirements for the degree of
Master of Science

LABORATORY MEASUREMENTS OF THE MOIST ENTHALPY TRANSFER COEFFICIENT

Dahai Jeong

Approved:

_____ Dr. Brian Haus Associate Professor of Applied Marine Physics	_____ Dr. Terri A. Scandura Dean of the Graduate School
_____ Dr. William M. Drennan Associate Professor of Applied Marine Physics	_____ Dr. Mark A. Donelan Professor of Applied Marine Physics
_____ Dr. Shuyi S. Chen Professor of Meteorology and Physical Oceanography	

JEONG, DAHAI (M.S., Applied Marine Physics)

Laboratory Measurements of the Moist Enthalpy Transfer Coefficient (August 2008)

Abstract of a thesis at the University of Miami.

Thesis supervised by Professor Brian Haus.
No. of pages in text. (63)

The enthalpy (sensible and latent heat) exchange processes within the surface layers at an air-water interface have been examined in 15-m wind-wave tunnel at the University of Miami. Measurements yielded 72 mean values of fluxes and bulk variables in the wind speed (referred to 10 m) range form 0.6 to 39 m/s, covering a full range of aerodynamic conditions from smooth to fully rough. Meteorological variables and bulk enthalpy transfer coefficients, measured at 0.2-m height, were adjusted to neutral stratification and 10-m height following the Monin-Obukhov similarity approach. The ratio of the bulk coefficients of enthalpy and momentum was estimated to evaluate Emanuel's (1995) hypothesis. Indirect "Calorimetric" measurements gave reliable estimates of enthalpy flux from the air-water interface, but the moisture gained in the lower air from evaporation of spray over the rough water remained uncertain, stressing the need for flux measurements along with simultaneous spray data to quantify spray's contribution to the turbulent air-water enthalpy fluxes.

ACKNOWLEDGEMENTS

I would like to acknowledge the Office of Naval Research for supporting my work under grant number N00140610258.

I would like to thank my advisor Dr. Brian Haus for his patience and warm heart while dealing with his first graduate student. His professional guidance allowed me to feel comfortable and confident to voice my ideas and opinions about the project.

Dr. William Drennan and Dr. Mark Donelan also had a great impact on me during my graduate program so far acting as committee members as well as scientific mentors and motivators. I would also like to thank Dr. Shuyi Chen for bringing her prospective to my work serving as the outside member of my committee.

Without the support of the faculty, staff, and students of both Applied Marine Physics and the Rosenstiel School I would not have been able to complete my work. I would especially like to thank Ivan Savelyev for his amazing help and teaching in the wave tank, as well as Jun Zhang for all his discussions and scientific insight. I also thank Michael Rebozo and Manuel Collazo for all their technical assistance setting up the tank for my experiments.

Finally, but most importantly, my family. I would like to thank my parents for their love, encouragement to go after my dreams, and for giving me the tools to achieve them. And my husband for his endless support not only as a romantic partner, but as an insightful scientific colleague.

TABLE OF CONTENTS

LIST OF FIGURES

LIST OF SYMBOLS

c_l = specific heat of liquid water

c_{pd} = specific heat capacity of dry air at constant pressure

c_{pl} = specific heat capacity of water at constant pressure

c_{pv} = specific heat capacity of water vapor at constant pressure

c_p = specific heat of air at constant pressure

C_D = drag coefficient

C_E = bulk humidity flux coefficient (Dalton number)

C_H = bulk temperature flux coefficient (Stanton number)

C_K = bulk enthalpy flux coefficient

e_s = saturation vapor pressure (hPa)

g = acceleration due to gravity

H_K = enthalpy flux

H_L = humidity (latent heat) flux

H_S = temperature (sensible heat) flux

k = moist enthalpy

K = eddy diffusivity

L = fundamental surface-layer length scale (Obukhov length)

L_v = latent heat of vaporization

p = pressure (hPa)

q = fluctuation of specific humidity

q_* = fundamental surface-layer humidity scale

Q = mean specific humidity

Q_s = surface mean specific humidity

Q_{10N} = neutral 10 m mean specific humidity

R_v = specific gas constant for water vapor

t = fluctuation of air temperature

t_* = fundamental surface-layer temperature scale

t_v = fluctuation of virtual temperature

t_{v*} = virtual temperature scale

T = mean air temperature

T_d = dew-point temperature

T_s = surface mean air temperature

T_v = mean virtual temperature

T_w = bulk water temperature

T_{10N} = neutral 10 m mean air temperature

u = fluctuation of downwind velocity

u_* = fundamental surface-layer velocity scale (friction velocity)

U_{10N} = mean neutrally stable 10 m wind speed

w = fluctuation of vertical wind velocity

z = height of observation

z_Q = roughness length for humidity

z_T = roughness length for temperature

z_0 = roughness length

κ = von Kármán constant (=0.4)

ρ = air density

ρ_l = density of liquid water

τ = momentum flux

ϕ_h = non-dimensional scalar gradient

ϕ_m = non-dimensional wind speed gradient

ψ = stability correction

ζ = non-dimensional stability parameter

Chapter 1

Introduction

Transfer of momentum, mass and sensible heat across the air-sea interface plays an important role in numerous geophysical phenomena. Cyclonic storm development, upper ocean mixing, and wave growth are examples. For instance, evaporation of water from the ocean is one of the important processes in controlling upper ocean temperature. Surface evaporative cooling and simultaneous increase in salinity lead to a buoyancy flux in the upper ocean that stimulates vertical motion and mixing in the near-surface waters. In the atmosphere, water vapor is distributed both vertically and horizontally by air currents, and latent heat is eventually released to the atmosphere through condensation during cloud formation and precipitation. This thermal energy is a basic energy source for atmospheric motions.

Air-sea interfacial turbulent fluxes are especially important in the formation and development of hurricanes. Tropical storms draw their energy from latent and sensible heat release in the eyewall and return some of it back to the sea through drag on the sea surface. Hence storm modeling requires accurate knowledge of the air–sea fluxes. Air–sea fluxes, however, being relatively difficult to measure, are rarely available outside dedicated campaigns. Consequently, models rely on parameterizations of the fluxes in

terms of more readily available parameters. Typically the fluxes are given in terms of bulk coefficients. For instance the momentum flux (or wind stress; that is vertical transport of horizontal momentum) is parameterized in terms of the mean neutrally stable 10-m wind speed U_{10N} and the air density ρ via the drag coefficient C_D as:

$$\tau = C_D \rho U_{10N}^2 . \tag{1.1a}$$

Similarly the latent (or humidity) and sensible heat fluxes are given, respectively, by

$$H_L = C_E \rho L_v U_{10N} (Q_s - Q_{10N}) \tag{1.1b}$$

$$H_S = C_H \rho c_p U_{10N} (T_s - T_{10N}) . \tag{1.1c}$$

Here C_E and C_H are the bulk humidity and temperature flux coefficients (or Dalton and Stanton numbers), respectively and are height dependent, c_p is the specific heat of air (at constant pressure), L_v is the latent heat of vaporization, Q_{10N} and Q_s are the neutral 10 m and surface mean specific humidities, respectively, and T_{10N} and T_s are the neutral 10 m and surface mean air temperatures, respectively.

Emanuel (1986, 1995), using a simple axisymmetric hurricane model, finds that the maximum predicted wind speed is proportional to the ratio of the bulk coefficients of moist enthalpy and momentum, C_K / C_D. Here moist enthalpy $k = \left[c_p (1-q) + c_l q \right] T + L_v q$, where T is the air temperature, c_l the specific heat of liquid water. Assuming the bulk humidity and sensible heat coefficients to be equal, as is verified for low to moderate wind speeds, C_K can taken to be equal to C_E and C_H. Based on the comparison of model predictions with observations, Emanuel finds the most likely range of the C_K / C_D ratio is 1.2 to 1.5, with a lowest bound of 0.75. For $C_K / C_D < 0.75$ the energy lost to drag

exceeds that gained from enthalpy, and tropical storms die down. However as can be determined from existing bulk flux relations, $C_E / C_D \approx 0.5$ for $U = 20$ m/s and no actual measurements of C_K / C_D have been previously reported for wind velocities greater than 20 m/s to evaluate this hypothesis (Zhang 2007).

After three decades of air–sea turbulence flux measurements (e.g., Smith 1980, Wu 1980, Anderson and Smith 1981, Large and Pond 1981, 1982, Smith et al. 1990, 1992, Webster and Lukas 1992, DeCosmo et al. 1996, Powell et al. 2003, French et al. 2007, Drennan et al. 2007), there is a general agreement on the behavior of the parameterizations of momentum, humidity, and heat fluxes at moderate wind speeds. The drag coefficients shown in Figure 1.1, an ensemble from six field and laboratory experiments and one modeling study, are typical of most recent campaigns. For moderate wind speeds of 5 to 20 m/s, it has been repeatedly shown that the drag coefficient increases nearly monotonically (e.g., Smith 1980, Large and Pond 1981, Smith et al. 1992, DeCosmo et al. 1996) with wind speed. However, the recent field and laboratory experiments of Powell et al. (2003) and Donelan et al. (2004) have shown that the expectation of increasing roughness with increasing wind speed, such as described by the generally used bulk drag transfer coefficients (e.g., Large and Pond 1981), finds a limit at wind speeds of tropical storms and hurricanes.

Humidity flux data are fewer than those of momentum flux due to the lack (until recently) of fast response hygrometers suitable for the marine environment. Dalton numbers from four field experiments and one modeling study are shown in Figure 1.2. Although the datasets show considerable scatter, there is no significant dependence of Dalton number with wind speed. Figure 1.2 is typical of existing humidity flux datasets in

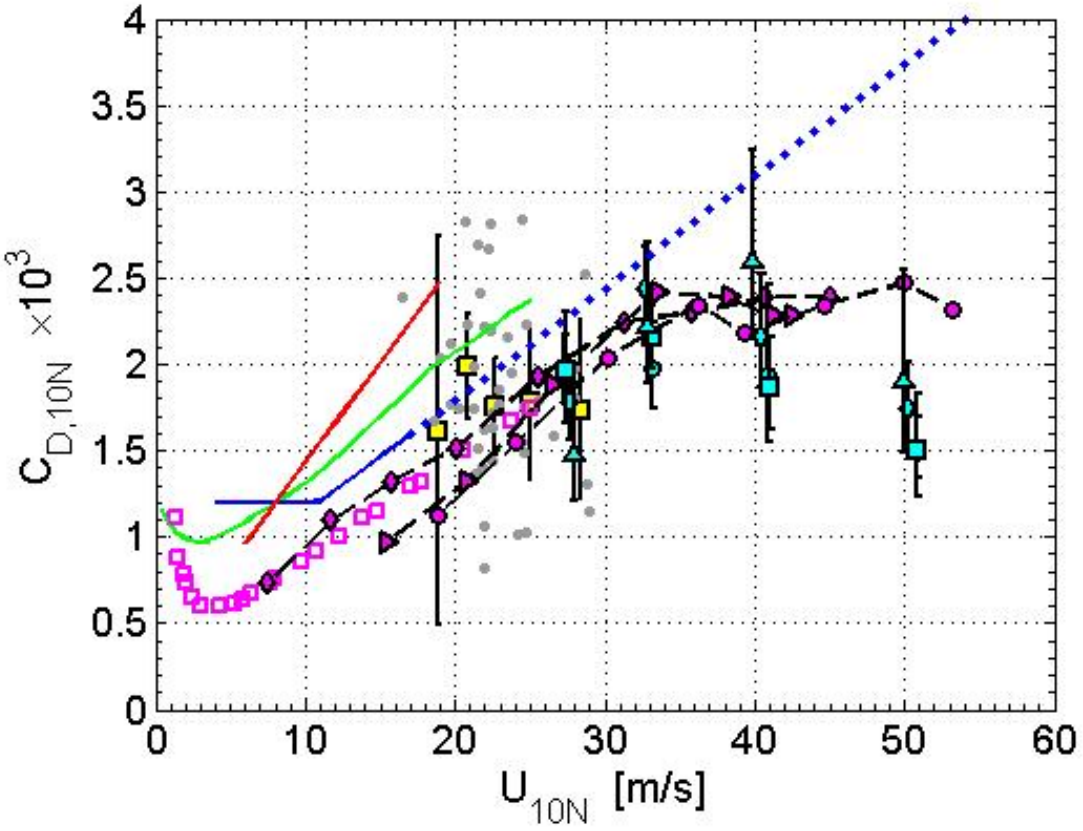

Figure 1.1. Plot of drag coefficient vs. wind speed at 10-m height for neutral stability, from six field and laboratory experiments and one modeling study. Shown are results from French et al. (CBLAST 2007; yellow squares and gray dots), Ocampo-Torres et al. (1994; magenta squares), Donelan et al. (2004; magenta diamonds, right-pointing triangles, circles), Powell et al. (2003; cyan squares, circles, diamonds, upward-pointing triangles), Fairall et al. (COARE 2003; green line), DeCosmo et al. (HEXOS 1996; red line) and Large and Pond (1981; blue line and extrapolated to high winds with dotted line). Vertical bars represent the range of estimates based on 95% confidence limits and symbols show estimates based on the depth of the surface layer used for the fit (Powell et al. 2003; cyan circles 10–100 m, squares 10–150 m, upward-pointing triangles 20–100 m, diamonds 20–150 m) and the methods used for stress measurement (Donelan et al. 2004; profile method, magenta right-pointing triangles; momemtum budget, circles; Reynold stress, diamonds).

that there are few direct air–sea flux measurements for wind speeds over 20 m/s. Hence the use of bulk relations in higher wind conditions requires extrapolating them well beyond their validated range and into a regime where enhanced wave breaking, sea spray, and bubbles may significantly change the transfer processes.

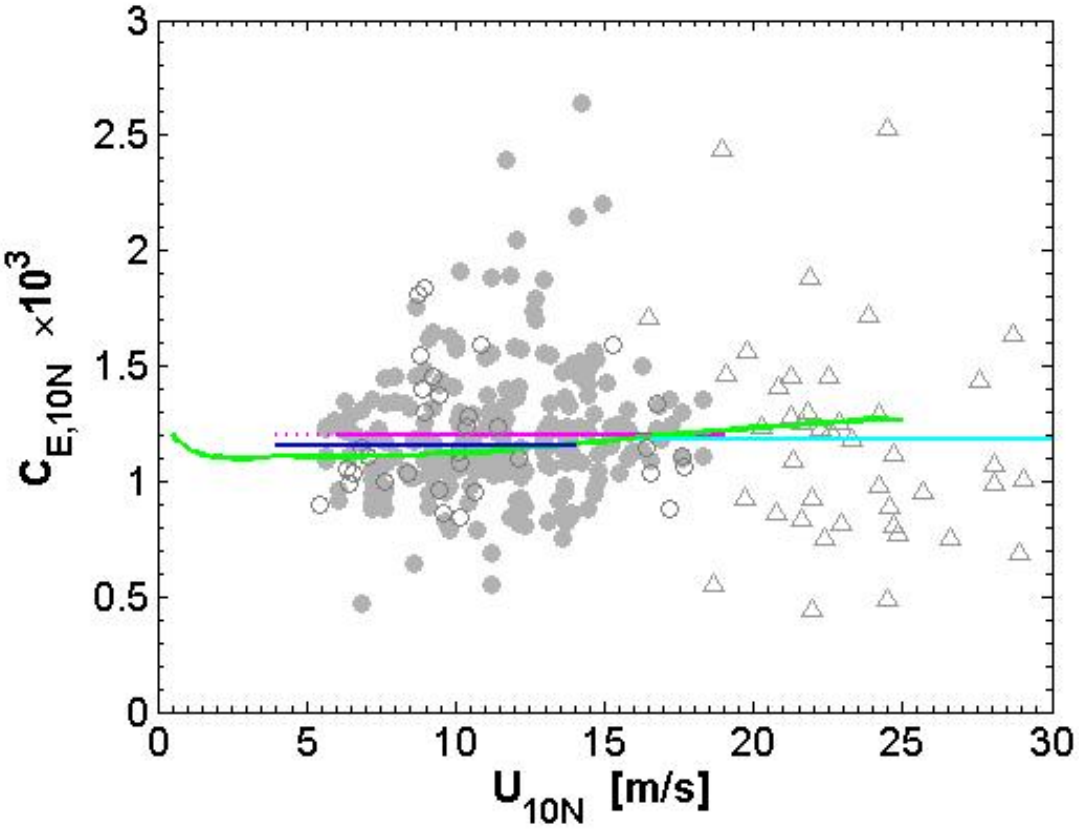

Figure 1.2. Plot of Dalton number vs. wind speed at 10 m height for neutral stability, from four field experiments and one modeling study. The HEXMAX data (Smith and Anderson 1988) points and mean value are shown with circles and magenta dotted line, respectively. The HEXOS data (DeCosmo et al., 1996), shown with gray circles and the magenta solid line, have been corrected according to Fairall et al. (2003). The CBLAST data (Drennan et al. 2007) shown with upward-pointing triangles and the cyan solid line. The blue solid line is the average of Large and Pond (1982). The green curve is from COARE 3.0 (Fairall et al., 2003).

Over the past few years, there has been a growing interest in increasing our understanding of high wind air–sea interaction processes. Powell et al. (2003) and Donelan et al. (2004) have recently shown that the drag coefficient levels off at wind speeds over 30 to 40 m/s. However, even with the leveling-off of the drag, the Emanuel criterion cannot be met without a corresponding increase in Dalton number. There remains the need for flux measurements in the high wind regime.

The experimental determination of transfer coefficients by direct "eddy correlation" (or covariance) flux measurements at sea is difficult, since turbulent flux data are inherently noisy and bulk meteorological quantities difficult to measure with sufficient accuracy. Such measurements from ships involve additional complications caused by ship motion, flow distortion, and the contaminating effects of the marine environment (e.g., Panofsky and Dutton 1984; Businger 1986; Wyngaard 1990). The flux data from field measurements, such as those reported in Figure 1.2, show large scatter and are incapable of revealing the underlying sources of variation of transfer coefficients. These circumstances suggest the need for complementing field measurements with laboratory studies carried out under controlled conditions, where the effect of every parameter on the exchange processes can be determined from imposed independent variations during laboratory experiments.

The objective of the present work is to advance our knowledge on the nature of the transfer process across the air-water interface, in particular in high winds. The work presented herein focuses on the measurements of enthalpy flux in the high wind regime. These data were obtained at the wind-wave facility at the Rosenstiel School of Marine and Atmospheric Science, University of Miami (Air-Sea Interaction Saltwater Tank - ASIST), where small-scale dynamic and thermodynamic air-sea exchange processes can be simulated. Following this introduction, Chapter 2 gives some general background on similarity relationships and bulk flux theory. Chapter 3 discusses measurements from the controlled laboratory environment. Chapter 4 presents analysis methods including data quality assurance and the computation of surface enthalpy fluxes. Chapter 5 presents

results and discusses these results in relation to other measurements. Chapter 6 provides some concluding remarks and suggestions for future work.

Chapter 2

Background

This chapter reviews both the theoretical and observational bases for our understanding of the mean structure of the Atmospheric Surface Layer (ASL), defined as the layer near the earth's surface in which the turbulent fluxes are approximately constant with height. Understanding this structure then allows estimating the turbulent surface fluxes of momentum and sensible and latent heat.

2.1 Monin-Obukhov Similarity Theory

Following scaling arguments, Monin and Obukhov (1954) recognized u_* and t_* as fundamental flux scales in the ASL, defined as

$$u_* = \sqrt{-\overline{uw}} \tag{2.1}$$

$$t_* = -\overline{wt} / u_* \tag{2.2}$$

where u_* is the fundamental surface-layer velocity scale, also known as the friction velocity, and t_* is the fundamental surface-layer temperature scale. u, w and t are fluctuations of downwind velocity, vertical velocity and temperature, respectively. u_* and t_* are constant with height in the ASL by Monin-Obukhov theory.

They also took the buoyancy parameter ratio g/T_v of inertia and buoyancy forces to be an important parameter, where g is the acceleration due to gravity and T_v is the mean virtual temperature. Lastly, they assumed the height of the observation, z, to be a fundamental length scale in the surface layer. Consequently, they hypothesized that all surface-layer statistics should scale with combinations of these four quantities.

We now know, however, that for scaling properties that depend on air density, rather than t_* alone, we need a scale that also includes the fundamental surface-layer humidity scale q_* (Zilitinkevich 1966)

$$q_* = -\overline{wq}/u_*. \tag{2.3}$$

where q is fluctuation of specific humidity. This is the virtual temperature scale, t_{v*}, defined as

$$t_{v*} = t_*(1+0.61\overline{Q}) + 0.61\overline{T}q_* \tag{2.4}$$

where $\overline{Q}$ and $\overline{T}$ must be layer-averaged mean specific humidity and temperature. Because t_* and q_* are constant with height in the surface layer, t_{v*} is too.

From u_*, t_{v*}, and g/T_v, it is possible to define a fundamental length scale L that is also a constant in the ASL

$$\frac{1}{L} \equiv -\frac{\kappa g(\overline{wt_v})}{T_v u_*^3} = \frac{\kappa g t_{v*}}{T_v u_*^2} = \frac{\kappa g}{\overline{T} u_*^2}\left(t_* + \frac{0.61\overline{T}}{1+0.61\overline{Q}} q_*\right) \tag{2.5}$$

where $\kappa\,(=0.4)$ is the von Kármán constant, and L is the Obukhov length.

On recognizing the dynamical significance of the surface layer scales u_*, t_*, z and L (we have since added t_{v*} and q_*), Monin and Obukhov (1954) speculated that all surface-layer turbulence statistics should behave similarly when properly expressed in terms of these scales (see also Businger 1973, Wyngaard 1973). In particular, Monin-Obukhov similarity quantifies stability effects in the ASL with the nondimensional stability parameter $z/L \equiv \zeta$. The Obukhov (1946) length, L, is the balance between shear-generated and buoyancy-generated or –suppressed turbulence, including both temperature and humidity related buoyancy effects. Thus, roughly when $|\zeta| > 1$, buoyancy effects dominate mechanical processes in the surface layer; when $|\zeta| < 1$, mechanical effects dominate. When $\zeta < 0$, the surface is heating and, thus, destabilizing the air in the ASL through the turbulent exchange of sensible and latent heat. This process creates unstable stratification. When $\zeta > 0$, the surface is extracting heat from the ASL and thereby cooling it from below. This results in a stably stratified ASL.

Monin-Obukhov similarity theory is the basic similarity hypothesis for the horizontally homogeneous surface layer. Theory predicts that all surface-layer flow properties can be expressed as dimensionless universal functions only of $\zeta\,(=z/L)$ when they are properly scaled. With these equations and the hypothesis that the fluxes in the surface layer are uniform with height, the momentum flux, sensible heat flux, and fluxes of water vapor and other gases can be determined. There have been many confirmations of Monin-Obukhov similarity theory (for reviews see Haugen 1973,

Panofsky and Dutton 1984), and it is now the foundation for our understanding of processes in the atmospheric surface layer.

2.2 Surface-Layer Profiles

2.2.1 Neutral Stratification

Long before the advent of Monin-Obukhov similarity theory, turbulence researchers used scaling arguments to model the wind speed profile in neutral stratification. u_* is the fundamental velocity scale in the ASL, and z is a fundamental length scale. In neutral stratification (i.e., when L is infinite or $\overline{wt_v}$ is zero), these are the only scales available to us. Consequently, the vertical gradient in wind speed must obey

$$\frac{dU}{dz} = \frac{u_*}{\kappa z} \tag{2.6}$$

where κ, the von Kármán constant, assures the equality.

The no-slip boundary condition means that $U(z)$ is zero at the surface. Hence, we can integrate Eq. 2.6 easily to obtain

$$U(z) = \frac{u_*}{\kappa} \ln z + b \tag{2.7}$$

where b is an integration constant. Because of the logarithm on the right side of Eq. 2.7, we cannot write $U(z=0)=0$. Rather, we define a new length scale, the roughness length z_0, where $U(z=z_0)=0$. Thus

$$b=-\frac{u_*}{\kappa}\ln z_0 . \tag{2.8}$$

Consequently,

$$U(z)=\frac{u_*}{\kappa}\ln(z/z_0) \tag{2.9}$$

the familiar semi-logarithmic form of the wind speed profile in neutral stratification.

Equation 2.9, however, is not just a theoretical construct. Semi-logarithmic wind speed profiles are fairly common in nature.

If $\overline{wt_v}$ is small enough that conditions are still near neutral though t_* (i.e., the sensible heat flux) is non zero, the temperature profile obeys the same scaling as in Eq. 2.6. Because t_* is the appropriate temperature scale

$$\frac{dT}{dz}=\frac{t_*}{\kappa z} . \tag{2.10}$$

There is no reason to assume that the same multiplicative coefficient κ^{-1} should appear in both Eq. 2.6 and 2.10. In fact, the experiments in Kansas (Businger et al. 1971) showed not only that $\kappa=0.35$ — rather than the more common value of 0.40 — but also that there should be an additional multiplicative constant of value 0.74 on the right side of Eq. 2.10. Wieringa (1980), however, reexamined the Kansas data, concluded that $\kappa=0.41$, nearly the traditional value of 0.40, and found no need for an additional multiplicative constant in Eq. 2.10. Högström's (1988) review suggested $\kappa=0.40\pm0.01$ and, again, that Eq. 2.6 and 2.10 represent correct scaling in neural stratification.

Henceforth, We take the more traditional but observationally defensible position that $\kappa = 0.40$ and that the von Kármán constant is the only factor necessary in both Eq. 2.6 and 2.10.

As we did with Eq. 2.6, we can integrate Eq. 2.10 from the surface to height z. The result is

$$T(z) = T_s + \frac{t_*}{\kappa} \ln z + c \tag{2.11}$$

where T_s is the surface temperature, and c is a constant of integration. As in Eq. 2.8, we find c by requiring T to be T_s at the surface; thus

$$T(z) = T_s + \frac{t_*}{\kappa} \ln(z / z_T) \tag{2.12}$$

where z_T is a new length scale, the roughness length for temperature.

Exactly the same arguments that we used to predict the temperature gradient also apply to specific humidity. Thus, in near-neutral stratification

$$\frac{dQ}{dz} = \frac{q_*}{\kappa z} . \tag{2.13}$$

Integrating this yields

$$Q(z) = Q_s + \frac{q_*}{\kappa} \ln(z / z_Q) \tag{2.14}$$

where z_Q is yet another length scale, the roughness length for humidity. z_0, z_T, and z_Q are not necessarily equal.

2.2.2 Including Stratification Effects

Because atmospheric stratification is rarely near neutral, it often affects the shape of surface-layer profiles. Thus, Eq. 2.6, 2.10 and 2.13, the log-linear profiles in neutral and near-neutral stratifications in which the effects of buoyancy are negligible, are not strictly accurate in diabatic conditions. We can extend these, however, on the basis of Monin-Obukhov similarity theory. These diabatic profile corrections, in fact, are at the core of Monin and Obukhov's (1954) work. They simply tried to retain the basic form of Eq. 2.6, 2.10 and 2.13 by multiplying these by functions that depend only on z/L; thus the flux-profile relations

$$\frac{dU}{dz} = \frac{u_*}{\kappa z}\phi_m(\zeta) \tag{2.15a}$$

$$\frac{dT}{dz} = \frac{t_*}{\kappa z}\phi_h(\zeta) \tag{2.15b}$$

$$\frac{dQ}{dz} = \frac{q_*}{\kappa z}\phi_h(\zeta) \tag{2.15c}$$

where ϕ_m and ϕ_h are non-dimensional wind speed, scalar gradients, respectively, and should be universal functions of ζ.

While Monin-Obukhov similarity theory predicts that ϕ functions should exist, it does not predict their functional forms. Ultimately, these ϕ functions — though presumably universal — are empirical: They must be found experimentally. Notice, the same ϕ function is used in both the temperature and humidity equations because there is no good theoretical reason why these should be different (Hill 1989). A definitive

experiment that verifies this assumption, however, has not been done, though several experiments support it (e.g., Dyer 1974, Dyer and Bradley 1982).

For unstable conditions, ϕ_m and ϕ_h are fairly well known (e.g., Paulson 1970)

$$\phi_m(\zeta) = (1-16\zeta)^{-1/4} \tag{2.16a}$$

$$\phi_h(\zeta) = (1-16\zeta)^{-1/2}. \tag{2.16b}$$

These are commonly called the Businger-Dyer relations because Joost Businger (1966) and Arch Dyer derived them independently in the mid-1960s (Businger 1988). Though

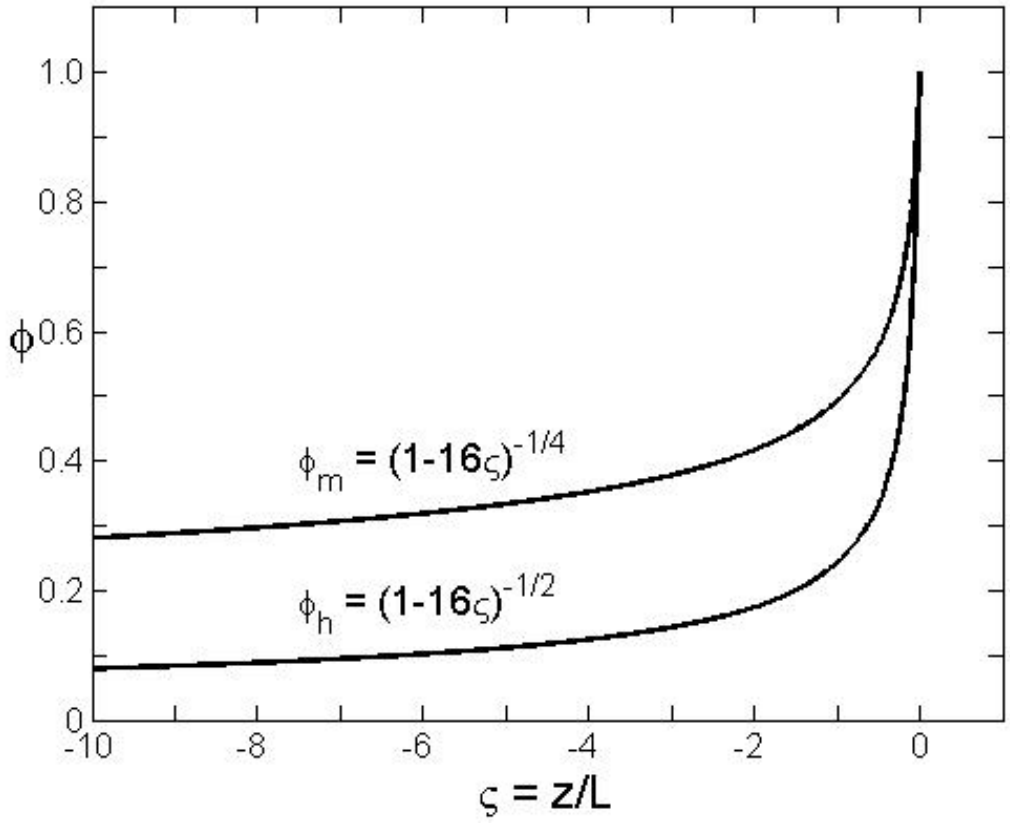

Figure 2.1. Nondimensional wind speed and scalar gradients, ϕ_m and ϕ_h, as function of stability for unstable conditions.

the constant multiplying ζ in Eq. 2.16 may vary somewhat among the various experimental evaluations of ϕ_m and ϕ_h (e.g., Dyer and Hicks 1970, Businger et al. 1971, Wieringa 1980, Dyer and Bradley 1982, Högström 1988), the same basic functional form comes through.

Figure 2.1 shows Eq. 2.16 as function of stability. Notice in the figure and in Eq. 2.16, $\phi_m = \phi_h = 1$ at $\zeta = 0$ (i.e., for neutral stratification) as Eq. 2.6, 2.10, and 2.13 require. Figure 2.1 also shows that as $-\zeta$ gets larger (as conditions become more unstable) both ϕ_m and ϕ_h decrease monotonically. This means, according to Eq. 2.15, that the vertical gradients of wind speed, temperature and humidity get weaker as the instability increases. The vertical exchange that the increasing buoyancy fosters homogenizes the profiles.

One, however, must be careful about the application of this simplified similarity theory to real marine atmospheric boundary layers, where processes aloft can affect the gradients associated with the larger scale motions and thus decouple the fluxes from the local surface boundary gradients.

We restrict our attention here to the unstable stratification, because all of the runs presented here were taken in unstable conditions. The interested reader is referred to, for example, Businger et al. (1971), Webb (1970), Dyer (1974), Large and Pond (1981), Wieringa (1980), Large and Pond (1982), Högström (1988) for a further discussion of the forms of ϕ_m and ϕ_h for stable stratification.

2.3 The Estimation of Surface fluxes

2.3.1 Direct and Indirect Flux Methods

In the atmospheric surface layer turbulent transport of momentum, heat, and water vapor is carried by fluctuations of the vertical wind. Over the past three decades specialized instruments (high-frequency response sensors) have been developed that allow direct determination of the turbulent fluxes by measuring fluctuations of all variables on the horizontal and temporal scales of interest. This is referred to as the covariance or "Eddy correlation" method, and is the only direct flux measurement:

$$\tau = -\rho\overline{wu} \tag{2.17a}$$

$$H_S = \rho c_p \overline{wt} \tag{2.17b}$$

$$H_L = \rho L_v \overline{wq} \tag{2.17c}$$

The overbar implies averaging over all relevant scales of the time variation of the fluxes. These formulas are strictly valid only in horizontally homogeneous conditions, and when the turbulence statistics are stationary (e.g. Busch 1972).

There are also many indirect approaches to flux estimation including the profile method and the inertial-dissipation method (e.g., Blanc 1985, 1987; Fairall and Larsen 1986; Edson et al. 1991). The turbulent fluxes can be estimated by measuring the vertical gradient in variables of interest and with the aid of an eddy diffusivity (or eddy transfer coefficient), K. This is referred to as the "Profile" method:

$$\tau = \rho K_m \frac{\partial U}{\partial z} \tag{2.18a}$$

$$H_S = -\rho c_p K_h \frac{\partial T}{\partial z} \tag{2.18b}$$

$$H_L = -\rho L_v K_e \frac{\partial Q}{\partial z} \tag{2.18c}$$

The profile method has recently found less application because of the difficulties in keeping instruments at different elevations well intercalibrated, particularly over the ocean where there are very small differences in T and Q over a feasible range of heights above the wave crests. Another difficulty with estimating fluxes from the slope of the profile is the modification of the profile just above the air-sea interface by surface waves (e.g., Hasse et al. 1978). The influence of the waves decays exponentially with height.

The "Inertial-dissipation" method uses characteristics of the inertial subrange of atmospheric velocity and scalar turbulence spectra that is normally observed at size scales between the production of turbulent kinetic energy (large scales) and the dissipation of energy (small scales). (e.g., Fairall and Larsen 1986, Edson et al. 1991). The method has the advantage of being less sensitive to platform motion than the eddy correlation method. More complete descriptions of flux methods can be found in Smith et al. (1996) or Fairall et al. (1997).

2.3.2 Bulk Algorithms

Turbulent surface fluxes, being relatively difficult, expensive and impractical to measure, are rarely available despite this diversity of flux methods. Consequently, for

estimating fluxes from field data, in numerical models, and for analytical studies, it is often convenient to know the so-called bulk transfer coefficients. Theses relate turbulent fluxes to more readily available quantities.

Bulk aerodynamic formulas are often used to calculate the surface fluxes. Here, I will discuss the bulk transfer coefficients for momentum (usually called the drag coefficient) and for sensible and latent heat. These are defined as in Eq. 1.1. The turbulent fluxes of momentum, heat, and water vapor can thus be estimated from measurements of mean quantities once the values of the exchange coefficients are established. To that end the left-hand side of Eq. 1.1 must be measured together with the mean quantities on the right-hand side. In the laboratory studies presented here, the "Calorimetric" method was used to estimate the surface heat transfer (the left-hand side of Eq. 1.1) by measuring the decrease of the heat content in the water as cooler air is blown over the surface (details are given in Chapter 3).

In the section 2.2.2, the gradient functions $\phi_m(\zeta)$ and $\phi_h(\zeta)$ were introduced in Eq. 2.15. These let us quantify U_{10N}, $T_s - T_{10N}$ and $Q_s - Q_{10N}$ in Eq. 1.1 and thereby provide a mathematical framework for handling the bulk transfer coefficients. Take wind speed as an example. Panofsky (1963) and Paulson (1970) showed how to integrate Eq. 2.15. The trick is to write

$$\frac{dU}{dz} = \frac{u_*}{\kappa z}[1-1+\phi_m(\zeta)]. \tag{2.19}$$

Then the integration becomes

$$\int_{U(z_0)}^{U(z)} dU' = \frac{u_*}{\kappa}\left[\int_{z_0}^{z}\frac{dz'}{z} - \int_0^{\zeta}\frac{1-\phi_m(\zeta')}{\zeta'}d\zeta'\right]. \tag{2.20}$$

Hence, because $U(z_0) = 0$

$$U(z) = \frac{u_*}{\kappa}[\ln(z / z_0) - \psi_m(\zeta)]. \tag{2.21}$$

Thus, the trick in Eq. 2.19 leads again to a semi logarithmic profile with an additive stability correction. That stability correction in Eq. 2.21, ψ_m, is defined as

$$\psi_m(\zeta) = \int_0^{\zeta} \frac{1-\phi_m(\zeta')}{\zeta'} d\zeta'. \tag{2.22}$$

We can follow exactly the same procedure with the temperature and specific humidity gradients in Eq. 2.15b and 2.15c to obtain the profiles of these variables

$$T(z) = T_s + \frac{t_*}{\kappa}[\ln(z / z_T) - \psi_h(\zeta)] \tag{2.23a}$$

$$Q(z) = Q_s + \frac{q_*}{\kappa}[\ln(z / z_Q) - \psi_h(\zeta)] \tag{2.23b}$$

where

$$\psi_h(\zeta) = \int_0^{\zeta} \frac{1-\phi_h(\zeta')}{\zeta'} d\zeta'. \tag{2.24}$$

The stability correction functions, ψ_m and ψ_h (Paulson 1970), that result from integrating the gradient functions, ϕ_m and ϕ_h (described in the section 2.2.2, Eq. 2.16) are

$$\psi_m(\zeta) = 2\ln\left(\frac{1+X}{2}\right) + \ln\left(\frac{1+X^2}{2}\right) - 2\tan^{-1} X + \frac{\pi}{2} \tag{2.25a}$$

$$\psi_h(\zeta) = 2\ln\left(\frac{1+Y}{2}\right) \tag{2.25b}$$

where

$$X = \left(1-16\zeta\right)^{1/4} \tag{2.26a}$$

$$Y = \left(1-16\zeta\right)^{1/2}. \tag{2.26b}$$

From Eq. 1.1, 2.21 and 2.23, we see that the bulk transfer coefficients have a dependence on surface stability prescribed by Monin-Obukhov similarity theory.

These equations (1.1 and 2.19 to 2.26) provide the necessary information to deduce the boundary stress and fluxes from observed difference, provided the neutral bulk transfer coefficients are known. Typical approaches are given by Hasse et al. (1978) and Large and Pond (1982).

Chapter 3

Experiments

The enthalpy (or heat content) exchange processes within the surface layers at an air-water interface have been examined in experiments in the wind-wave facility at the Rosenstiel School of Marine and Atmospheric Science, University of Miami. The components of the enthalpy flux are: 1) the direct turbulent transfer of "sensible" heat by the vertical movement of relatively cool or warm parcels of air, 2) the direct turbulent transfer of latent heat by the differential vertical motion of more or less moist air, 3) the transport and phase changes of spray droplets released from the surface, and 4) radiative transfer between various levels of the two fluids. In this work, 1,2 & 3 were examined through laboratory experiments. The objectives of the experiments are to repeat the workings of nature on a reduced scale, so that measurements taken can be scaled up to yield prototype information and to reveal the physics of the processes of the turbulent transfer of heat under controlled conditions.

In total, 103 enthalpy flux runs with the wind set to fixed speeds were made from Jun, 2006 to March, 2007. Data were taken at 0.2 m height with windspeeds ranging from

0 to 17 m/s (equivalent to 39 m/s at 10 m height) and water-air temperature differences ranging from 1.3 to 9.2 ºC. All the experiments were conducted in freshwater.

In this chapter the instrumentation and methods used to measure the turbulent moist enthalpy (sensible and latent heat) flux and the techniques employed for the conditions of high wind with spray are described.

3.1 The Facility and Experimental Setup

3.1.1 The Characteristics of the Air-Sea Interaction Facility

The Air-Sea Interaction Saltwater Tank (ASIST) at the University of Miami (Figure 3.1) has a test section that is 15 m long, 1 m wide and 1 m high; the water depth can be up to 0.5 m, leaving 0.5 m for air flow. It may be operated either closed ("circulating mode": The flume is tightly closed so that the air circulates continuously) or open ("ventilating mode"). The experiments reported here were conducted in the ventilating mode; the flume flaps were kept open so that air entered the flume from the outside of laboratory and, after one circuit, exited to the atmosphere (outside air). Air flow is produced by drawing air through the test section with a fan at the downstream end of the flume. Several small mesh screens (and a set of honeycomb ducts) in the inlet straighten and condition the air flow. The centerline wind speed (of the tunnel) can be programmed up to 30 m/s in circulating mode and 17 m/s in ventilating mode.

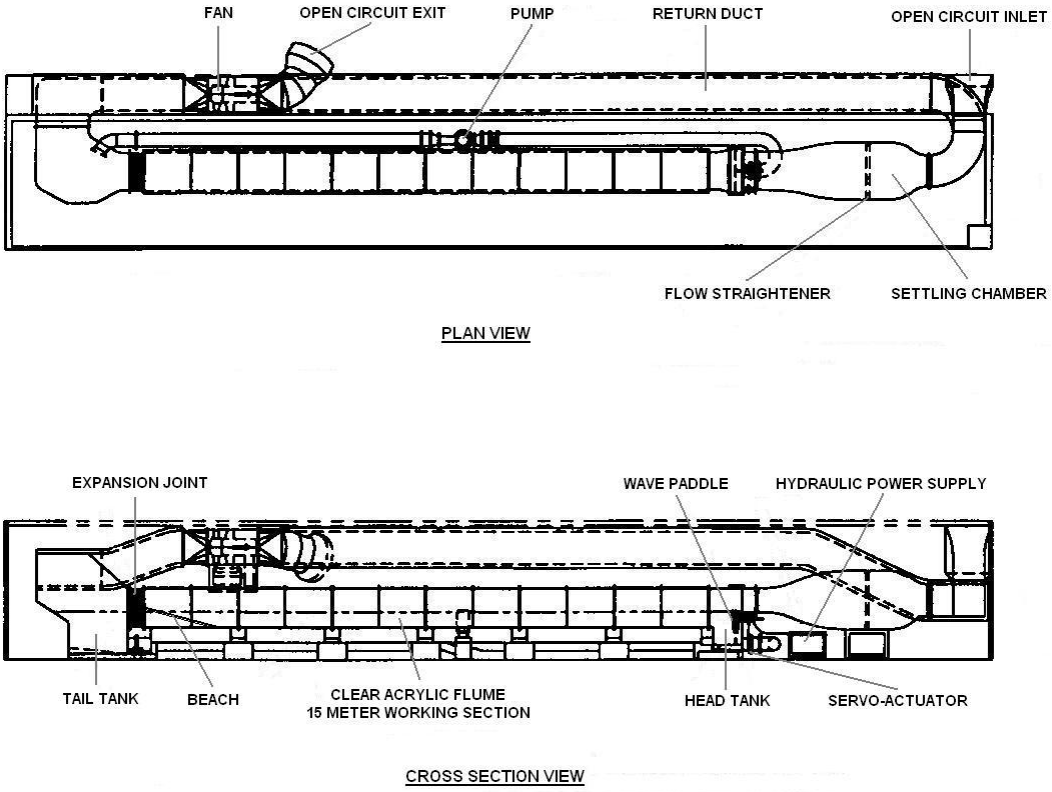

Figure 3.1. Schematic of the ASIST wind-wave flume facility.

At the maximum wind speed in ventilating mode wave breaking is intense and the tops of the wave crests are blown into spume. In the water a “beach” at the downwind end is used to minimize wave reflections into the test section. The working section is constructed of acrylic so that optical measurements may be made anywhere along the 15 m fetch.

A "tail" tank at the downwind end of the test section and a "head" tank at the upwind end are connected by a pipe which has an inline pump used to circulate and mix the water. A current of up to 0.5 m/s may be generated by this pump in either direction. The water can be heated or cooled by built in heat exchangers in the external pipe (with a

precision of around 0.1 ºC in time and space). The total water volume in the tank and pipe is about 9.7 m^3 with a water depth of 0.42 m in the test section for the experiments reported here.

3.1.2 Dynamic Similarity to the Field

Turbulent transfers can be modeled effectively in a wind-water tunnel in which a turbulent interfacial boundary layer forms when a controlled airflow blows over a water reservoir. To achieve similarity with field mechanisms, the dynamic structure of the lowest layers of the atmosphere and the uppermost layers of the ocean must be properly simulated. The main dimensionless parameters, which provide criteria for determining dynamic similitude, to consider are (1) the Reynolds number, the dimensionless ratio of inertial to viscous forces, which must be large ($>10^5$); (2) the Richardson number, the dimensionless ratio of buoyant suppression of turbulence to shear generation of turbulence, which must approach unity to generate stable or unstable conditions; and (3) the Froude number (the nondimensional ratio of inertial to gravity forces) and wave age, which must cover a sufficiently large range of values to ensure the occurrence of realistic wind-wave coupling effects.

The flexibility of the ASIST facility allows the above conditions to be fulfilled. The possibility to achieve a simulation of the turbulent transfer mechanisms in the laboratory facility is thus supported. Furthermore, the ASIST, wherein both dynamic and thermodynamic exchange mechanisms can be simulated at the same time, permits to

study of mutual interactions between different transfer mechanisms. Limitations inherent to any laboratory modeling must, however, be kept in mind. As a consequence, the extension of the model results to the natural situation requires careful theoretical reasoning and in situ verifications.

3.1.3 Experimental Set-up

In this work, there were three instrumented measuring stations (Figure 3.2) in the ASIST. These are referred to as station 1, 2, and 3, respectively, at the upwind end (0.38 to 2.93 m), 5.9 m from the upwind end, and the downwind end (11.78 to 15 m) of the test section. Sensors placed at both stations 1 and 3 are (a) thermistors (1560 Black Stack, Hart Scientific) to measure mean air and bulk water temperatures, and (b) a closed-path infrared analyzer (LI-6262, LI-COR) to determine mean specific humidity. At station 2, a Pitot static tube was used to measure wind speed (free-stream air velocity) at a height 0.2 m. An infrared camera (radiometer) (ThermaCAM^{TM} SC 3000, FLIR Systems) was also used at station 2 to measure the surface temperature (thereby, the value of the saturation water vapor pressure at the surface temperature for humidity). At station 3, the probe for air temperature was mounted in a protective tube with forced aspiration to avoid contamination of the sensor by spray droplets.

The analog signals, humidity and wind speed, were digitized and recorded at 25 Hz. Water and air temperature were monitored and recorded every 5 seconds.

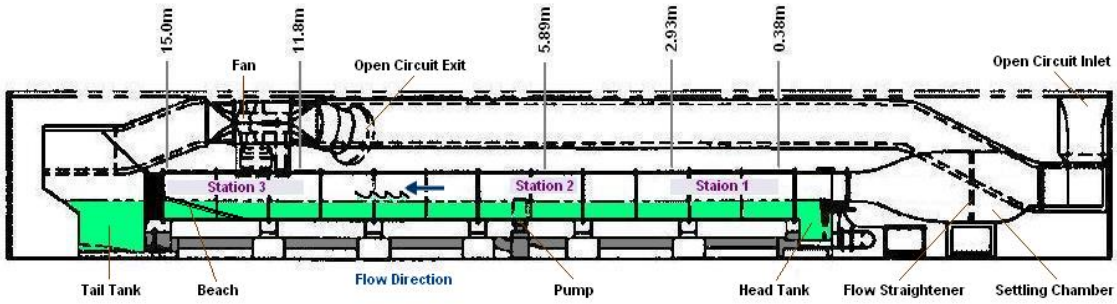

Figure 3.2. Diagram of the test section of the wind-wave flume.

3.2 Experimental Procedure for Enthalpy Flux Runs

At the start of each constant wind speed run, the water was heated using heat exchangers in the external pipe while the inline circulation pump was operated at a rather high speed (0.4 to 0.5 m/s) thereby rapidly mixing the entire water mass. The wind was maintained at low speed to keep the concentration of water vapor in the air at the ambient outside air level as the initial condition. When the specified water temperature was reached, the heat exchanger was shut off, the water pump slowed down to 0.08 m/s, and once the water velocity stabilized, the wind was set to a specified speed to begin the data gathering. The length of the experiments varied between 15 and 40 min, depending on wind speed.

Special attention was paid to the temporal and spatial stability of the flow to ensure repeatable and comparative experiments. A rigid plate was placed at the entrance section of the water tank, providing a smooth transition between the inlet air and the water surface.

3.3 The Instrumentation and Methods

3.3.1 Surface Enthalpy Flux Measurements: The Calorimetric Method

One of fundamental difficulties with the direct flux measurement (covariance or “Eddy correlation” method) in a wind-water tunnel at high wind speeds is the chance of spray droplets falling on hot-film anemometer probes, corrupting the velocity data and possibly causing damage to the heated films. After much preliminary work to find a compromise between scientific interest and technical constraints, it was found that the calorimetric use of the tank provides accurate estimates of the surface enthalpy transfer but no direct separation of the sensible and latent parts of the flux.

The heat content change in the water was, therefore, determined by precisely measuring the rate of bulk change in the water temperature, the heat capacity of the tank contents, and the water surface area in steady winds. This is referred to as the "Calorimetric" method. Here the cooling rate of the water was measured with 2 thermistors placed at the upstream and downstream ends of the water tank respectively, while the water was continuously circulated at a slow speed (0.08 m/s) to assure that the water column was well mixed. The heat budget (loss) of water, however, does not only represent the enthalpy flux since the room temperature (hence the surface temperature of the tank walls and water pipes) was not kept the same as the temperature of the water thereby contributing the energy lost by radiative and conductive transfer to the heat budget. Thus, the radiative and conductive transfers were measured to normalize the estimates (and infer the enthalpy transfers).

In order to determine the effect of the temperature difference between room and water on the measurements of enthalpy fluxes, several runs were performed at a fixed current speed (0.08 m/s) and various temperature differences with an insulating cover installed over the water surface (hence no turbulent fluxes) (Figure 3.3). Figure 3.4 shows an example of the measured temperature during such a run. Polynomial fits to the water temperature measurements (solid line in Figure 3.4) yield estimates of the effect of the temperature difference between room and water on the total heat loss. These estimates are taken to be the radiative and conductive induced enhancements of heat loss and are subtracted from all the estimates of total heat loss (derived from the cooling rate of the water (dashed line in Figure 3.4) during flux runs). In the case of the flux run shown in Figure 3.4, this correction is 10 %. Details of the process of calculating the enthalpy fluxes are given in Chapter 4.

Figure 3.3. The insulating cover installed over the water surface.

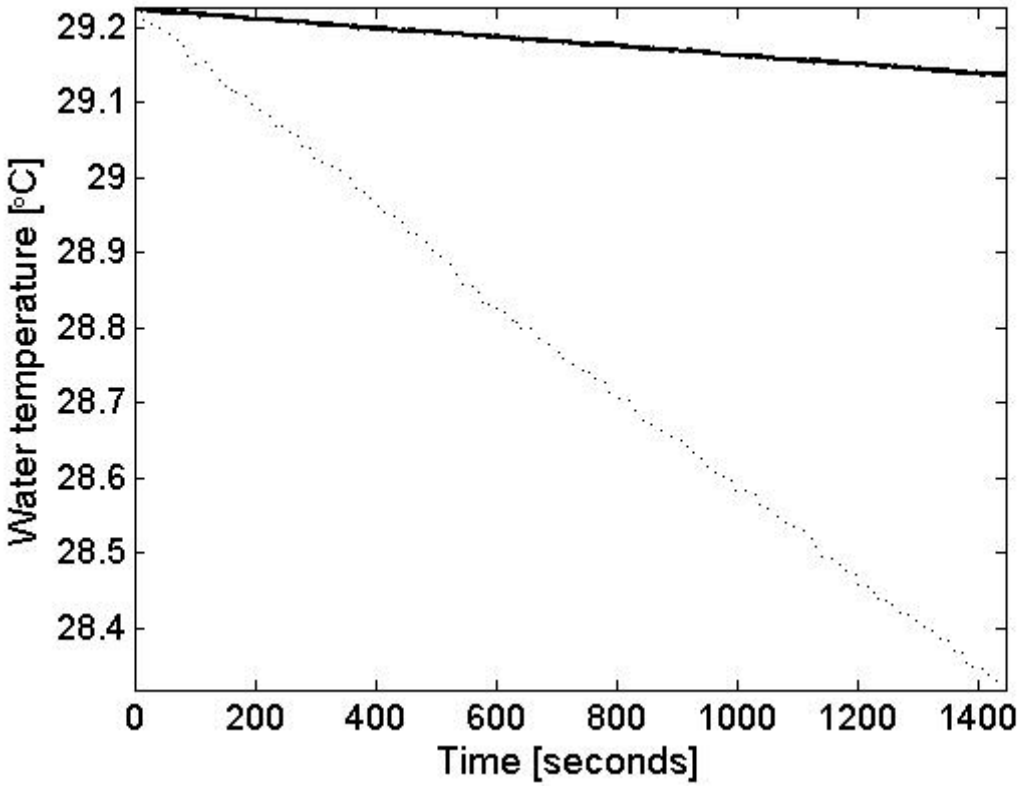

Figure 3.4. An example of the measurement of radiative and conductive heat transfers. The upper solid line is the water temperature in an experimental run with an insulating cover installed over the water surface, while the lower dotted line is the water temperature in a run with same conditions except without the insulating cover. Solid line yields estimate of the radiative and conductive heat loss, while dotted line yields estimate of the total heat loss.

3.3.2 Wind Speed Measurements

Wind velocities were measured with a standard Pitot-static tube at a sampling rate of 25 Hz. Measurements were made at a height of 0.2 m and a fetch of 5.9 m to minimize influences of wave and spray. Note that the free stream air velocity outside of the boundary layer is independent of fetch in the tunnel. The reason is that ASIST is carefully designed to make sure that the air flow is a boundary layer flow with near zero pressure

gradient, and that the air channel has a sufficient height to prevent pressure feed back from the wind waves (hence no blockage) (e.g., Plate 1965, 1978). The Pitot-static tube's differential pressure transducer was calibrated using a Chattok gauge.

3.3.3 Temperature Measurements & Spray Removal Technique

Mean air and bulk-water temperatures were measured by the "1560 Black Stack" thermistor system (Hart Scientific) with accuracy of 0.002 ºC. Two Black Stack systems each with two thermistor sensors were installed at fetches of 0.38 m and 11.78 m in the 15 m long test section; the built-in sampling control block allowed two thermistor sensors, which were connected to the system simultaneously, to measure the air and bulk-water temperature alternately with the sampling interval of 2.5 seconds, thereby avoiding cross calibration errors. At both fetches, the bulk water temperature measurements were made at a depth of 0.22 m in the 0.42 deep water flow section. At a fetch of 0.38 m, the air temperature measurements were made at a height of 0.38 m in the 0.58 thick air flow section. At a fetch of 11.78 m, the air temperature sensor, thermistor probe, was housed in an aspirated protective unit and the measurements were made as air from the flume is continuously pumped out through a ceiling port into the protective housing to avoid spray contamination of the sensor; the protective unit is a 30 cm long tube, 3 cm in diameter and built of acrylic so that visual inspections for accumulation of water droplets may be made.

The spray contamination problem may be explained as follows. In conditions of high winds with spray, evaporation of water droplets deposited on the thermistor probe cools the sensor, thereby producing a "cold spike" in the data. This process adds spurious variance to the time series of temperature, which is nearly impossible to remove since the amount of contamination can change during a data run.

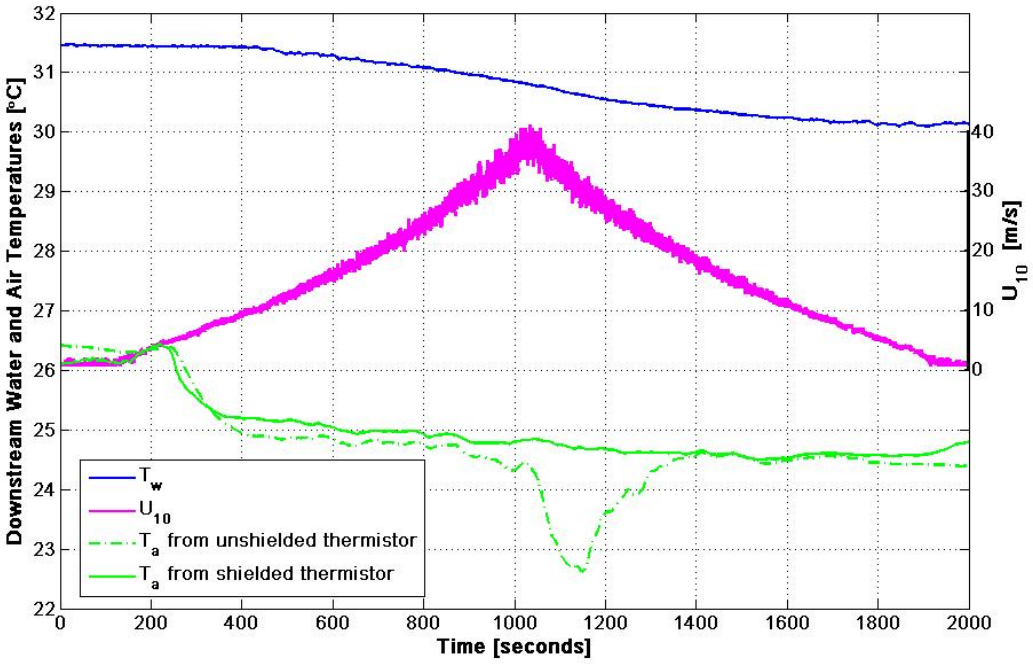

Figure 3.5. The changes in air and water temperatures during a run in which the wind speed was increased from 0 to its maximum (about 40 m/s referred to 10 m height) and decreased again to 0 (magenta line). The blue line at the top is the downstream water temperature; the green solid line is the downstream air temperature from the shielded thermistor sensor, while the green dash-dot line is the downstream air temperature from the unshielded thermistor sensor. The contamination of temperature sensor by spray is reflected in the sudden drop in downstream air temperature data from the unshielded sensor.

Figure 3.5 shows the comparison of data from shielded and unshielded thermistor sensors (respectively, a sensor inside the aspirated protective tube mounted on a ceiling

port and an unprotected sensor at 0.38 m above the water surface, both at a fetch of 11.78 m) during a 20 minute run in which the wind speed is ramped up from 0 to its maximum (about 40 m/s referred to 10 m) and down again. Comparison shows that the device (tube) appears to be effectively protecting the sensor from contamination by impacting spray droplets (advected by the horizontal wind), and the flow through the tube is slow enough that no thermodynamic heating effect (induced by motor-driven suction) is noticeable: this rather low flow rate was found to be adequate for measurements of mean temperature.

The temperature required in (1.1c) is the interfacial temperature of the water that is in direct contact with the air. Because the sensible, latent, and longwave radiative fluxes are carried out in the upper fractions of a millimeter of the surface, they lead to a "cool skin," this has been long recognized (Woodcock 1941, Saunders 1967). Typical bulk thermometers placed in the water to make contact temperature measurements are usually unable to resolve this thin layer. Therefore, the surface skin temperature was measured with an infrared camera system (ThermaCAM^{TM} SC 3000, FLIR Systems), which can measure the actual interface temperature precisely (e.g., Schluessel et al 1990, Coppin et al 1991, Emery et al 1994). Images were taken at 1 Hz with the camera mounted vertically on ceiling (hence at a distance to the water surface of 0.58 m) giving a field of view of 20º × 15º (41 cm × 30.6 cm). It was found that the difference between the bulk and the surface skin temperatures was negligible within the sensitivity of temperature sensors, confirming that the water column was well mixed.

3.3.4 Humidity Measurements

Mean specific humidity was measured with "LI-6262" gas analyzer (LI-COR), a closed-path, non-dispersive, infrared (NDIR) gas analyzer, at fetches of 0.38 m and 11.78 m in the 15 m long test section. In this instrument the water vapor concentration measurements are based on the difference in absorption of infrared radiation passing through the sample and reference cells. Measurements were made as air from the flume is continuously pumped out through a ceiling port into the flowmeter (Cole Parmer) in which moist air from the flume was diluted 20% with dry air (pure Nitrogen) to prevent condensation in the optical path of the gas analyzer, and then into the analyzer sample cell. The "LI-6262" gas analyzer was calibrated using a "LI-610" dewpoint generator (LI-COR).

Chapter 4

Data Analysis

In total, 103 enthalpy flux experiments were carried out with the wind set to fixed speeds. However, as the air temperature sensor at the fetch of 11.78 m was unshielded from spray droplets for the first 24 runs and was not operational during 7 other runs, data from these runs were not used in the analysis. A total of 72 suitable enthalpy flux runs were, therefore, included in the final analysis.

The turbulent flux of moist enthalpy (the flux driven by differences in temperature and water vapor density between the surface and the air) was measured indirectly by the "Calorimetric" method (the measurement of the amount of heat lost by warmer water body). As in earlier discussion, estimating fluxes from field data and in numerical models typically rely on bulk parameterizations, with 10 m as the standard reference height. To calculate the neutral 10 m bulk transfer coefficient, in addition to the surface fluxes, the bulk mean temperature difference $T_s - T_{10N}$, the bulk mean humidity difference $Q_s - Q_{10N}$, and mean wind speed U_{10N} are needed. This chapter provides the process of estimating these quantities and the moist enthalpy fluxes, and thereby gives estimates of the bulk transfer coefficients.

4.1 Estimates of the Surface Flux of Moist Enthalpy

Each run produces a time series of bulk water temperature (T_w). Figure 4.1 shows an example of the measured temperature during a run with 9.9 m/s wind (equivalent to 16 m/s at 10 m height). Polynomial fit to the bulk water temperature allows a continuous estimate of the total heat loss. Hence, it provides an estimate of the surface flux of moist enthalpy (H_K)

$$H_K = c_{pl}\rho_l \frac{\partial T_w}{\partial t}\frac{V_w}{A} \tag{4.1}$$

where c_{pl} is the specific heat capacity of water at constant pressure, ρ_l is the density of liquid water, $\partial T_w / \partial t$ represents the time derivative of the bulk water temperature, A is the surface area of the air-water interface exposed to the wind (15 m^2), V_w is the total volume of water (9.7 m^3).

As in earlier discussion, conductive and radiative transfer (heat transfer to surroundings through walls of tank and pipes), however, can cause an enhancement of total heat loss. This unwanted (and unavoidable) source of such heat transfer is that produced by a difference in temperature between the water and the laboratory. In order to estimate the conduction and radiation to surroundings, several runs were made at various water-room temperature differences with an insulating cover installed over the water surface (hence no surface fluxes); details of the measurements were given in Chapter 3 and illustrated by Figure 3.3 and 3.4. Polynomial fits to the water temperature measured during such runs yield estimates of the conduction and radiation by the same procedure in Eq. 4.1. These estimates are taken to be enhancements of total heat loss induced by water-

room temperature difference and are subtracted from all the estimates of total heat loss derived from Eq. 4.1. The corrected values are the estimates of H_K.

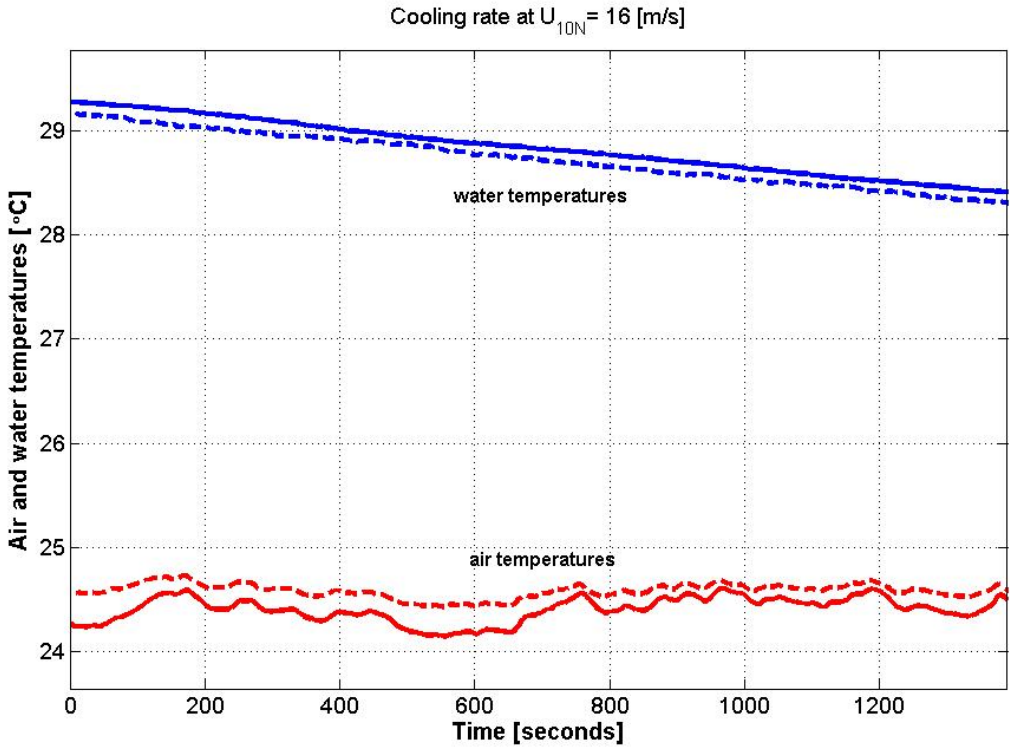

Figure 4.1. A time series of the bulk water and air temperature. The solid curves are the upstream water and air temperatures respectively, while dashed curves are the downstream water and air temperatures respectively. Polynomial fit to the water temperature yields estimate of total heat loss.

4.2 The Neutral 10 m Variables

4.2.1 Wind Speed, U_{10N}

The 10 m neutral wind is estimated from the wind measured at height z (0.2 m) by assuming a logarithmic mean wind profile with a stability correction as

$$U_{10N} \equiv \frac{u_*}{\kappa}\ln\left(\frac{10}{z_0}\right)$$

$$= U(z) - \frac{u_*}{\kappa}\left[\ln\left(\frac{z}{10}\right) + \psi_m(\zeta_{10}) - \psi_m(\zeta_z)\right] \qquad (4.2)$$

here u_* is calculated as per Donelan et al. (2004). The wind profile relations are a set of coupled equations (Eqs. 2.5, 2.25, 2.26, and 4.2) that are solved iteratively for the 10 m neutral wind and the stability; the initial stability is set to 0.

4.2.2 Specific Humidity, Q_{10N}

As the "LI-6262" measures dew-point temperature (T_d in ºC) (Figure 4.2), and not specific humidity, the specific humidity Q (kg/kg) is obtained according to

$$Q = \frac{0.622 e_s}{p - 0.378 e_s} \qquad (4.3)$$

where e_s is the saturation vapor pressure (hPa)

$$e_s = 6.11 \exp\left[\frac{L_v}{(R_v \times 273.16)} \frac{T_d}{(T_d + 273.16)}\right] \tag{4.4}$$

and p is the pressure in hPa and R_v is the specific gas constant for water vapor. The surface humidity Q_s is estimated from the same procedure with the surface temperature (cool skin) T_s in Eq. 4.3 and 4.4, assuming saturation. Figure 4.3 shows an example of the measured surface skin temperature using the infrared camera system.

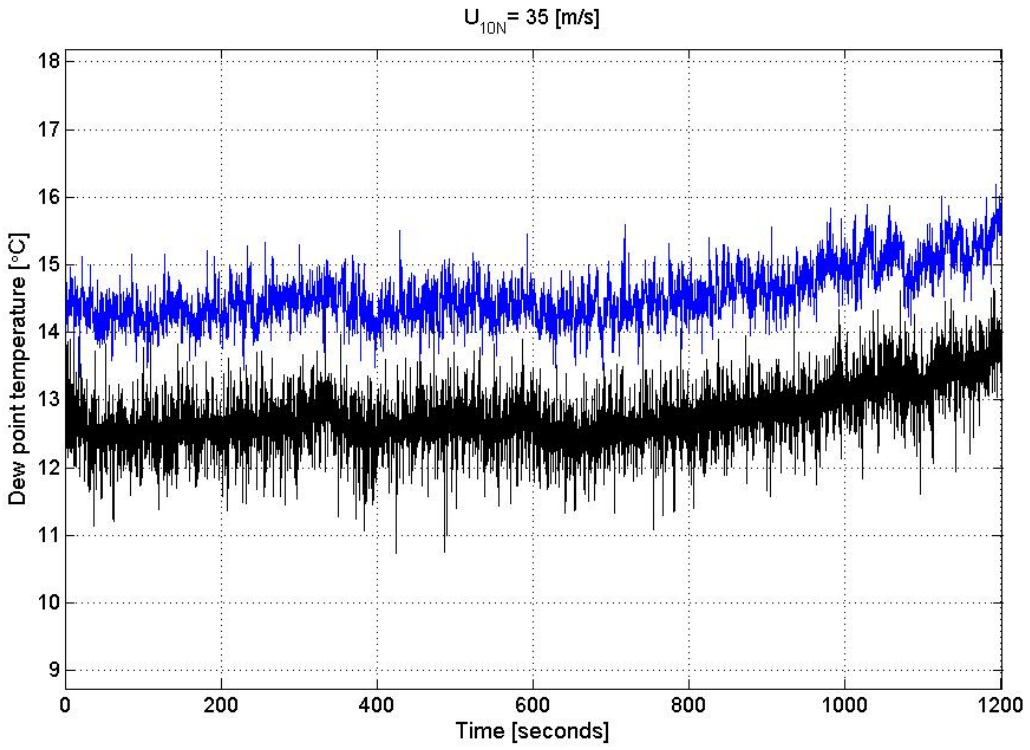

Figure 4.2. Time series of the dew point temperature signal (smooth version using a running average (5 points)). The upper blue curve is the downstream dew point temperature, while the lower black curve is the upstream dew point temperature.

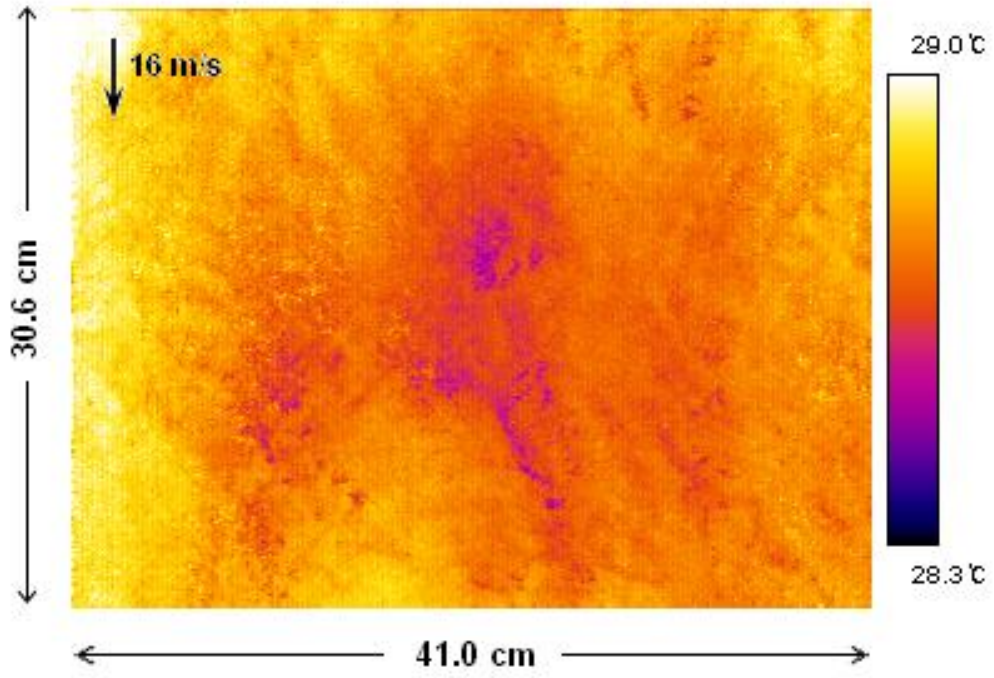

Figure 4.3. Image from IR camera of surface temperature.

The same arguments used to estimate the 10 m neutral wind also apply to specific humidity. Thus, the 10 m neutral specific humidity is computed from the specific humidity measured at height z (0.58 m) as

$$Q_{10N} \equiv Q_s + \frac{q_*}{\kappa}\ln\left(\frac{10}{z_Q}\right)$$

$$= Q(z) - \frac{q_*}{\kappa}\left[\ln\left(\frac{z}{10}\right) + \psi_h(\zeta_{10}) - \psi_h(\zeta_z)\right] \qquad (4.5)$$

here the bulk-derived value of q_* is used (assuming $C_E = 1.2\times10^{-3}$, modified HEXOS result (DeCosmo et al. 1996) according to Fairall et al. (2003) which do not differ

significantly from $C_E = 1.18 \pm 0.07 \times 10^{-3}$ (Drennan et al. 2007), since no direct measurement of latent heat was made).

4.2.3 Air Temperature, T_{10N}

Exactly the same arguments used to estimate the 10 m neutral specific humidity also apply to air temperature. Thus, the 10 m neutral temperature is computed from the temperature measured at height z as

$$T_{10N} \equiv T_s + \frac{t_*}{\kappa} \ln\left(\frac{10}{z_T}\right)$$

$$= T(z) - \frac{t_*}{\kappa}\left[\ln\left(\frac{z}{10}\right) + \psi_h(\zeta_{10}) - \psi_h(\zeta_z)\right] \tag{4.6}$$

here t_* is also estimated from bulk algorithm by assuming $C_H = C_E$ $(=1.2\times10^{-3})$.

4.3 Estimates of Bulk Enthalpy Transfer Coefficient

In addition to the turbulent fluxes of moist enthalpy H_K estimated from Eq. 4.1, the wind speed U_{10N}, specific humidity difference $Q_s - Q_{10N}$, and the mean temperature difference $T_s - T_{10N}$ are quantified in Eq. 4.2, 4.5, and 4.6, respectively, and thereby allowing estimate of the 10 m neutral bulk enthalpy transfer coefficient C_K from

$$H_K = C_K \rho U_{10N} \left(k_s - k_{10N} \right) \tag{4.7}$$

where k is the specific enthalpy of moist air, defined as the total enthalpy of the dry air and the water vapor (the sensible heat and latent heat respectively), and may be expressed by assuming that no liquid water is present in the air as (e.g., Emanuel 1994)

$$k = ((1-q)c_{pd} + qc_{pv})T + L_v q + \text{constant} \tag{4.8}$$

where c_{pd} is the specific heat capacity of dry air at constant pressure, c_{pv} is the specific heat capacity of water vapor at constant pressure, and q is the specific humidity.

Chapter 5

Results and Discussion

To advance our understanding of scalar exchange processes at the air-water interface, in particular in high winds, a total of 72 suitable enthalpy flux runs were taken at winds equivalent to 0.6 to 39 m/s at 10 m height by calorimetric use of the ASIST. For purposes of calculating fluxes based on meteorological data, a bulk parameterization of the transfer rates in terms of wind speed is usually most convenient. This chapter shows estimates of the bulk transfer coefficients of moist enthalpy based on 10 m neutral wind speed, and provides intercomparisons of the results with model predictions and observations (including ship, platform, aircraft, or laboratory measurements using covariance or inertial dissipation methods) to establish the credibility and accuracy of the laboratory flux measurements.

5.1 The Transfer Coefficients of Moist Enthalpy

The measurements of the enthalpy coefficient referred to wind speed at 10 m (C_K) are summarized in Figure 5.1. The C_K varies between 0.00097 and 0.0021 for U_{10N} ranging from 0.6 to 39 m/s. At low wind speeds (before the initial wavelets begin to appear at about 2 m/s) the C_K increase toward lower wind speeds as is characteristic of aerodynamically smooth flow (Liu et al. 1979, Donelan 1990, Wu 1992, Ocampo-Torres et al. 1994).[1] Once waves begin to form the sheltering effect at the troughs between the roughness elements (or waves) would increase as the roughness height increases, thereby suppressing heat and mass transports as the wind increases (Liu et al. 1979). For $U_{10N} \geq 5$ m/s, the interface is fully rough,[2] turbulent transport is facilitated and the C_K thus increase with wind speed (as the roughness of the surface increases). For wind speeds between about 2 and 5 m/s the two opposing effects due to increase in roughness balance each other and a minimum of C_K is observed. C_K shows almost no change in the wind speed range of 15 to 25 m/s, and decreases slightly above that speed. No (significant) positive effect on C_K due to increasing spray in the wave boundary layer is observed. This might be because the analysis used in this study does not differentiate between evaporation from the water surface and subsequent evaporation

[1] The flow over a smooth surface; that is, the actual roughness elements on the surface are embedded in the laminar sublayer where turbulent motion is suppressed and molecular diffusion dominates. The roughness elements over the ocean are primarily surface gravity waves that are generated by the wind/stress.

[2] A surface with individual roughness elements higher than the laminar (viscous) sublayer; that is, irregularities on the surface are sufficiently large that the turbulent boundary layer reaches right down to the surface.

from spray droplets in the wave boundary layer, while the evaporation from the water surface is the only heat lost by water body measured to estimate the enthalpy flux.

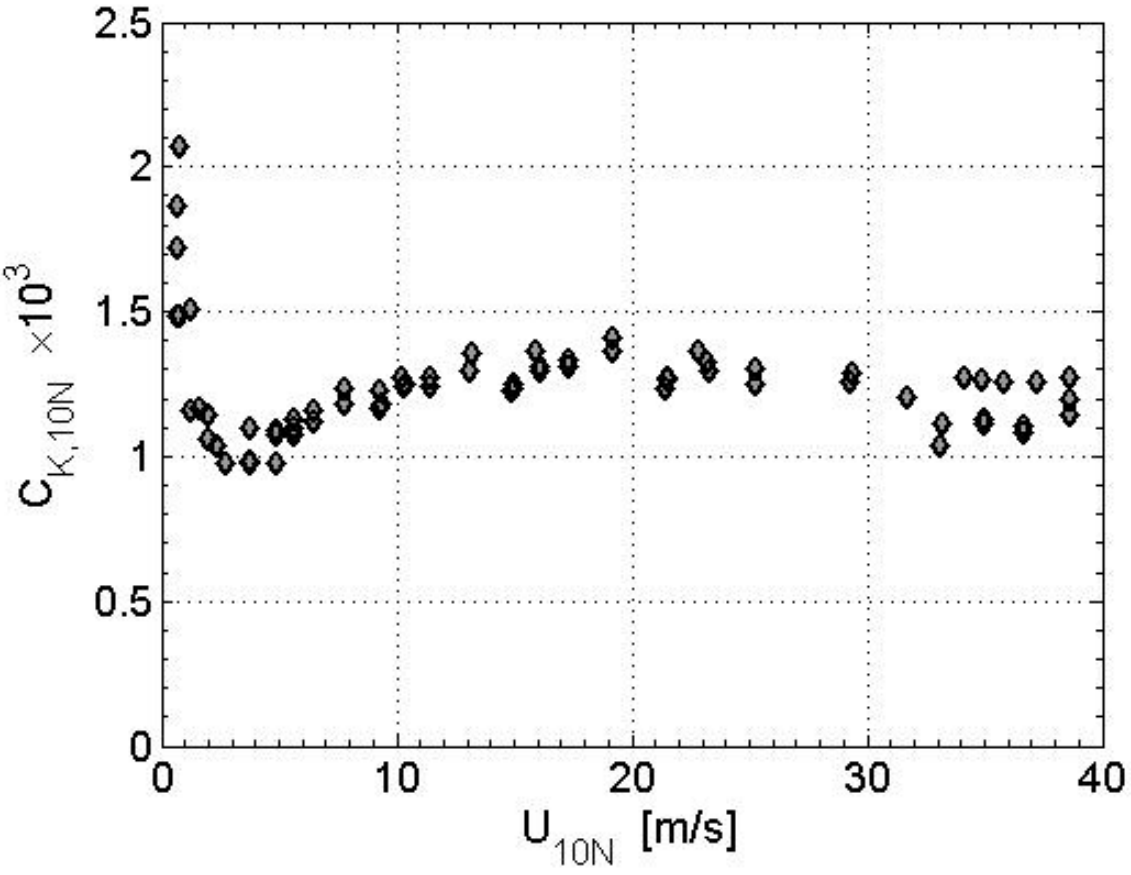

Figure 5.1. The enthalpy coefficient referred to wind speed at 10 m

In Figure 5.2, the characteristic behavior of the C_K (as the surface condition goes from aerodynamically smooth to rough) is compared to that of the C_D obtained in ASIST (Donelan et al. 2004). When the interface is smooth, momentum, heat and water vapour are all transported by molecular processes near the interface and the variations of C_D and C_K (should) share the same characteristics. At higher winds (rough flow

regime), the C_D increase more rapidly than the C_K. This might be expected because momentum can be transported by viscous shear and pressure forces on the roughness elements, while molecular diffusion is the only process which transports heat and mass at the interface when the interface is rough.

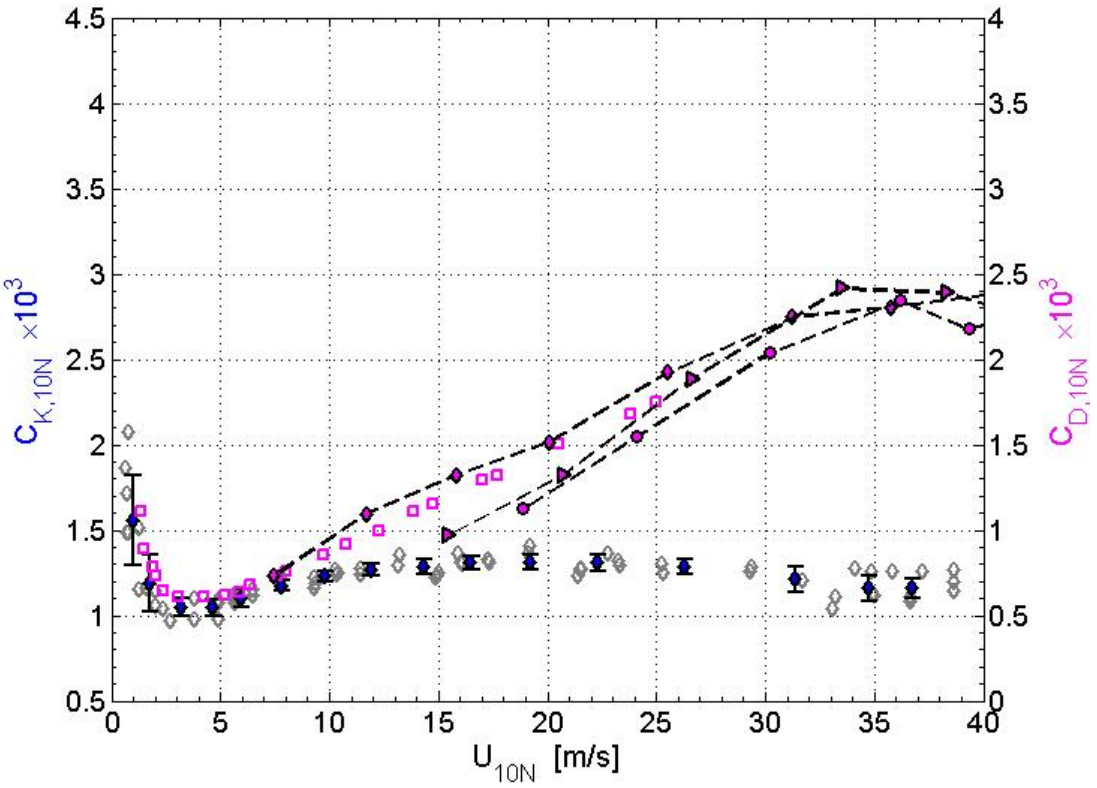

Figure 5.2. Comparison between the characteristic behaviors of enthalpy and drag coefficients; Present work (enthalpy coefficients; gray and blue diamonds; vertical bars represent the range of estimates based on 95% confidence limits), from Ocampo-Torres et al. (1994; drag coefficients; magenta squares), and from Donelan et al. (2004; drag coefficients; magenta diamonds, right-pointing triangles, circles)

5.2 Comparison with the Bulk Transfer Coefficients for Latent Heat from another Laboratory Study

There are a number of laboratory studies that measured either sensible heat (convection) or latent heat (evaporation) contributions to the enthalpy flux. However, there are no C_K measurements which included both contributions. In Figure 5.3, the results of evaporation measurements made from a different tank (The CCLW Gas Transfer Flume (GTF), 32.2 m × 0.76 m × 0.85 m) by Ocampo-Torres et al. (1994) are, therefore, compared to the value of C_K obtained in this laboratory study. Although GTF is longer than ASIST, an inverted beach (obstacle to waves) was installed for the experiments reported here, dividing the effective fetch into two (approximately 14 m and 18 m respectively), in such a way that GTF can be considered to have similar fetch values of the wave field in ASIST. Comparison between C_E and C_K (obtained in GTF and ASIST respectively) shows good agreement at low and moderate wind speed, as (might be) expected since the transfer process for heat and mass (should) share the same characteristics when no significant wave breaking and spray are yet present. This verifies the assumption that the transfer coefficients for latent heat (C_E) and sensible heat (C_H) are equal in magnitude and wind speed dependence for low to moderate winds (DeCosmo et al. 1996). For wind speed higher than 20 m/s, the GTF C_E shows a tendency to increase, while the ASIST C_K shows almost no change in the wind speed range of 15 to 25 m/s, and decreases slightly above that speed. This distinction between two cases might be due to the differences between the methods used to estimate fluxes. GTF experimental

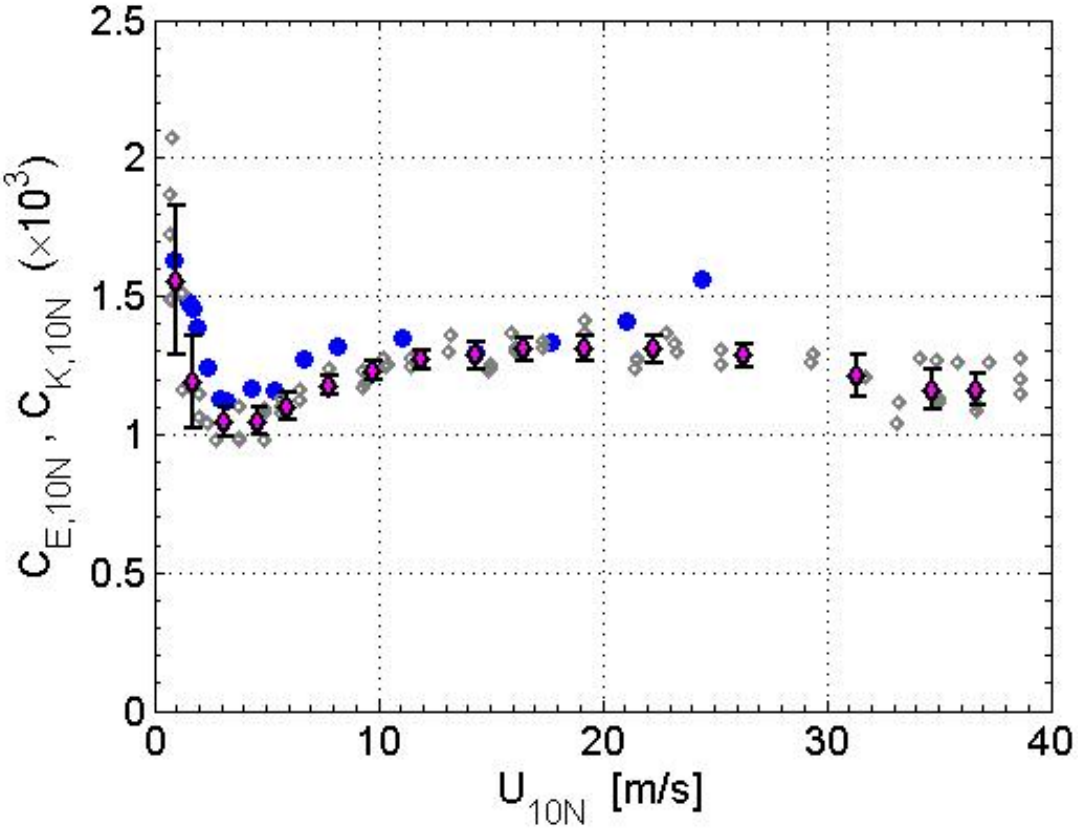

Figure 5.3. Comparison of enthalpy coefficient with the Dalton number from another experiment; Present work (C_K; gray and magenta diamonds), and from Ocampo-Torres et al. (1994; C_E; blue circles). Vertical bars represent the range of estimates based on 95% confidence limits.

approach was to determine an overall mass transfer rate for the whole flume by closing the flume ("circulating mode") and monitoring the build-up of water vapor, thereby measuring both evaporation from the surface and spray droplets in the wave boundary layer to estimate fluxes. As in earlier discussion, the evaporation from the water surface is, however, the only mass transfer measured to estimate the fluxes in the calorimetric ASIST measurements.

5.3 Comparison of C_K with Field Measurements

Figure 5.4 compares the results presented above with field measurements of enthalpy exchange coefficients produced by two different experimental groups. During the Humidity Exchange over the Sea (HEXOS) Main Experiment, the water vapor and sensible heat flux data (DeCosmo et al. 1996) were measured with the eddy correlation method from a platform, aircraft, and mast in the North Sea over the wind speed range 6 to 18 m/s. To make the published HEXOS results consistent with other measurements presented here, they were modified to account for three established correction factors (Fairall et al. 2003) including the following: 1) reduction in seawater vapor pressure by 2% due to salinity, 2) a true air–water interface temperature (i.e., cool skin corrected), and 3) the Webb correction (Webb et al. 1980) that considers the influences of the density fluctuations and the non-vanishing vertical wind component.[1] These changes increased their transfer coefficients by about 8%. Here enthalpy exchange coefficients are calculated based on the modified HEXOS sensible and latent heat flux data.

Direct (covariance) measurements of enthalpy exchange coefficients (Drennan et al. 2007, Zhang et al. 2008) were obtained during the Coupled Boundary Layer Air Sea Transfer (CBLAST) flights through Hurricanes Fabian and Isabel in 2003 over wind

[1] The total vertical flux of an air constituent (e.g., H_2O, CO_2) includes the turbulent vertical flux as well as the mean vertical flux (which is the vertical transport caused by the mean vertical flow). Usually, the mean flux is neglected for continuity reasons and the turbulent flux is considered to represent the complete constituent flux. This simplification, however, does not hold generally for the following reason (Webb et al., 1980). Turbulent motion consists of ascending and descending air parcels, which have different densities (ascending air parcels are less dense than descending air parcels). In order to maintain the mass balance, the vertical velocities of ascending parcels have to be different from that of descending ones. From this it follows that there is a mean vertical velocity that is different from zero. Hence, the turbulent flux obtained from eddy covariance measurements has to be corrected to give the total constituent flux by using the so-called 'Webb correction'.

speeds from 16 to 29 m/s. It is clear that there is much more scatter or variance in the CBLAST data than the earlier, lower wind (HEXOS) datasets. The high variability is explained by the short duration runs (typically 5 minutes) and high altitudes (O(100 m)) imposed by the operational need for clear air.

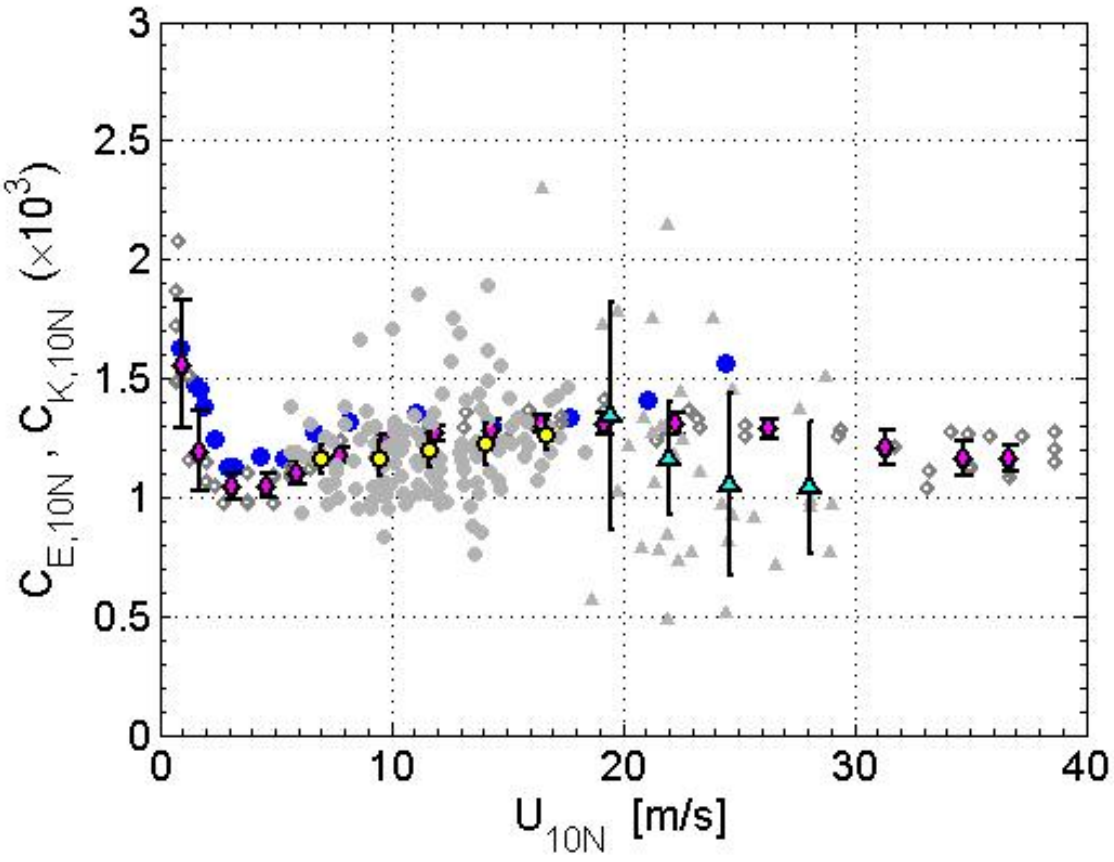

Figure 5.4. Comparison of enthalpy coefficient with the results from other experiments; Present work (C_K ; gray and magenta diamonds), Ocampo-Torres et al. (1994) (C_E ; blue circles), DeCosmo et al. 1996 (C_K ; gray and yellow circles), and from Zhang et al. 2008 (C_K ; gray and cyan upward-pointing triangles). Error bars indicate the 95% confidence interval of the bin average.

The scatter in the direct (covariance) field measurements is such that the details of the variations of C_K are obscured. The interest is, therefore, in the average performance

of the exchange coefficients, with information on its statistical scatter about the observations. Figure 5.4 shows comparisons of enthalpy coefficients averaged in bins of 10-m neutral wind (by bin averaging, reliable estimates of the variation of the mean C_k with wind speed were obtained). The bin width increases slightly at the higher wind speeds with sparse data. Error bars indicate the statistical uncertainty (95% confidence interval) of the bin-average based on the distribution within the wind speed bin. Most of the 95% confidence intervals on both the HEXOS and CBLAST C_K encompass the calorimetric ASIST tank measurements. In the range of wind speeds of 5 to 20 m/s the ASIST C_K agree particularly well with the field measurements. The compatibility of the laboratory measurements (ASIST and GTF results) with the field estimates of C_K (the platform and aircraft-based HEXOS and CBLAST data) is encouraging and establishes the validity and accuracy of the laboratory flux measurements and present (calorimetric) method.

The positive spray effect on C_K is expected to be significant at high winds (Wu 1979, Fairall et al. 1994, Makin 1998, Andreas and Emanuel 2001). It is evident that the ASIST and CBLAST data do not support such an increase in C_K. For wind speeds greater than 20 m/s, in fact the CBLAST data have a slight but insignificant negative slope with wind speed, while the GTF C_K increases and ASIST C_K shows almost no change. We note though that the percent of breaker coverage in ASIST (increases with $U_{10N}{}^3$ for winds from 7 to 35 m/s with a maximum of about 8 % as determined by a two-dimensional imaging of surface curvature) is consistent with aerial whitecap coverage estimates during CBLAST (Black et al. 2006). As in earlier discussion, the nature of

ASIST "calorimetric" method, that can not differentiate evaporation of spray droplets in the wave boundary layer (and cooling caused by subsequent spray re-entrained to water) from evaporation from the water surface, prohibit any firm conclusions on the effect of spray. Consequently, measurements at heights within and above the spray layer and direct measurements of the source of spray droplets are needed to sort out these effects.

5.4 The Ratio of the Moist Enthalpy and Surface Friction Coefficients

The ratio of the moist enthalpy and drag coefficients is thought to be of critical importance for hurricane forecasting, providing a limit on the maximum potential intensity (MPI) of a storm. Simple box models of the energy balance (Emanuel 1995) have suggested that values of C_K / C_D of order 1 are required for intense hurricanes to form. Similarity arguments (Emanuel 2003) have also suggested that these coefficients should become independent of wind speed in hurricanes.

Figure 5.5 shows the comparisons of the ratio of the enthalpy and drag coefficients to evaluate these hypotheses. The ASIST ratio is parallel but higher than those of the revised COARE relationship (Fairall et al. 2003) and the HEXOS values at winds lower than 20 m/s, and it matches the CBLAST ratio at higher winds. This figure shows the ratio from both laboratory and field measurements are well below the threshold value for intense hurricanes to form as suggested by maximum potential intensity theory. Furthermore in high winds ($U_{10N} \geq$ about 33 m/s), the ratio is invariant with wind speed up to the maximum winds measured. This might suggest self-similarity of the limiting

boundary layer processes and raise questions about our present understanding of the mechanisms that control hurricane intensity.

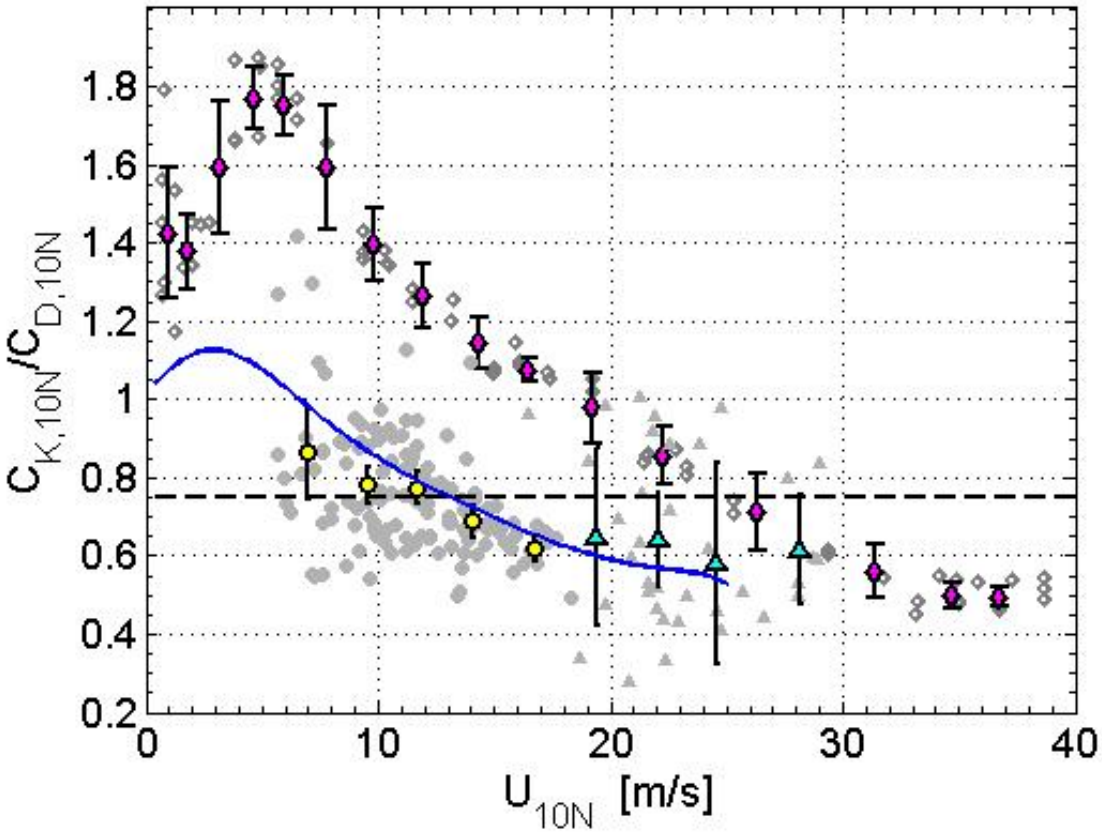

Figure 5.5. Comparison of the ratio of the enthalpy and drag coefficients with the results from other experiments; Present work (gray and magenta diamonds), Fairall et al. 2003 (blue solid line), DeCosmo et al. 1996 (gray and yellow circles), and from Zhang et al. 2008 (gray and cyan upward-pointing triangles). Error bars indicate the 95% confidence interval of the bin average. The threshold value of 0.75 suggested by Emanuel is also shown as the dashed line.

Given the close agreement for C_K (Figure 5.4), in particular for $U_{10N} < 20$ m/s, it is clear that the difference in C_K / C_D at moderate winds can be attributed mainly to C_D, which is lower in ASIST than in the field. This is expected because laboratory

observations of C_D have previously shown lower values than field observations in low to moderate winds (Figure 1.1), likely due to the significantly smaller fetch values of the wave field in a laboratory relative to the real ocean surface (Donelan et al. 2004).

To isolate the effect of C_D, the ratio was recalculated based on the ASIST C_K and a commonly used (COARE 3.0; Fairall et al. 2003) bulk algorithm C_D (which is based on the physical concepts of air-sea exchange and tuned to fit field measurements including HEXOS data) up to a wind speed of 30 m/s and a constant value thereafter (Powell et al. 2003). The corresponding results for the recalculated ratio are shown in Figure 5.6. The modified ASIST ratio shows a much improved agreement with the COARE and HEXOS observations. The ratios were essentially unchanged for winds above 30 m/s. The ratio values hold closely to a level of about 0.5 (below the critical level of 0.75 which had been suggested as a lower limit on the value in the high wind region of hurricanes in the context of the MPI) for winds greater than 30 m/s up to the maximum observed winds. The MPI limit for the ratio value 0.5 is only about 45 m/s (Emanuel 2003), suggesting that either there is a significant change in the ratio at winds greater than 40 m/s or the structure of the hurricane eye-wall and vortex dynamics depart from the simplified model structures. In fact, supports for the latter of these alternatives are provided by recent higher spatial and temporal resolution simulations (Persing et al 2003) and observations of mesovortices in the eye of Hurricane Isabel when it was a Category 5 storm (Montgomery et al. 2006). However, flux measurements (a combination of numerical, laboratory, and field studies) along with simultaneous sea spray data at high winds (even higher than present maximum observed winds) are needed in order to test the above hypothesis and to understand the role of sea spray.

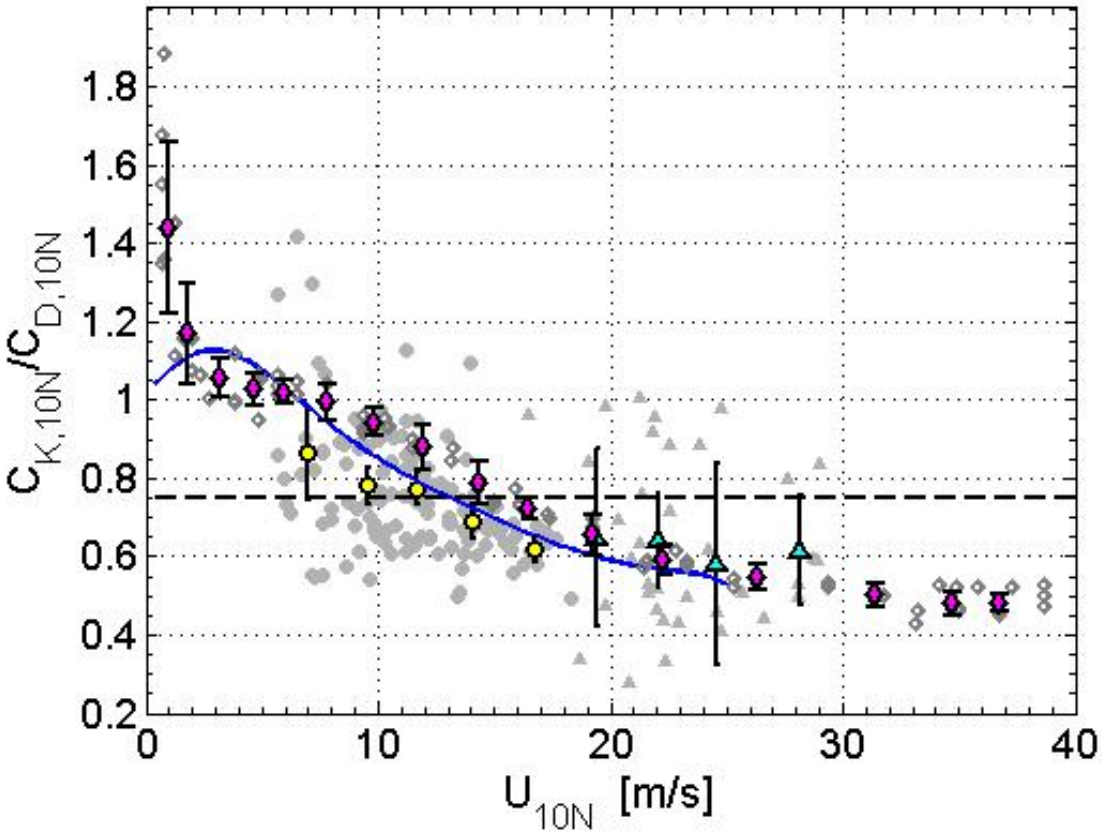

Figure 5.6. Comparison of the modified ratio of the enthalpy and drag coefficients with the results from other experiments; Present work (gray and magenta diamonds), Fairall et al. 2003 (blue solid line), DeCosmo et al. 1996 (gray and yellow circles), and from Zhang et al. 2008 (gray and cyan upward-pointing triangles). Error bars indicate the 95% confidence interval of the bin average. The threshold value of 0.75 suggested by Emanuel is also shown as the dashed line.

Chapter 6

Conclusions

In this study indirect "Calorimetric" measurements of enthalpy (sensible and latent heat) flux within the surface layers at an air-water interface were presented. Measurements were made at the Air-Sea Interaction Facility at the University of Miami. Values for enthalpy flux and bulk enthalpy transfer coefficients, measured at 0.2-m height, were adjusted to neutral stratification and 10-m height with 10-m neutral wind speeds from 0.6 to 39 m/s. The conclusions of this thesis are as following:

1. The development of a protective aspirated shield for the temperature sensor has made it possible to obtain high-quality measurements of mean air temperature over the water in conditions of high winds with spray.

2. On the basis that C_K is often represented as a constant value between 5 and 30 m/s, our measurements may be summarized by a value 1.25×10^{-3}, close to several other recent observations. However, our measurements clearly indicate that C_K increases steadily with wind speed from about 1.05×10^{-3} at 5 m/s to 1.3×10^{-3} at 15 m/s and no significant variation with wind speed is found at winds greater than 15 m/s.

3. For wind speeds up to 20 m/s, the results agree well with data from several

earlier studies. For wind speeds greater than 20 m/s, C_K is slightly less than values inferred from laboratory measurements (Ocampo-Torres et al. 1994) and slightly larger than aircraft measurements (Zhang et al. 2008). But, because of the absence of measurement of spray evaporation in the wave boundary layer in this study and the highly variable nature of the other field measurements, we are not able to provide a definitive verification of the behavior of C_K at high wind speeds where wave breaking and spray are present.

4. For wind speeds from 16 to 29 m/s, our measurement values of C_K and C_D (Fairall et al. 2003) yield a C_K / C_D ratio of 0.61, close to the value of 0.63 inferred from the aircraft measurements (Zhang et al. 2008), but significantly below the 0.75 threshold for hurricane development suggested by Emanuel (1995). This suggests that either there should be a significant change in the ratio at winds greater than maximum observed winds, or the Emanuel model assumptions should be revisited.

5. Although the present results increase the wind speed range for enthalpy flux measurements up to 39 m/s, the effect of spray on C_K is not yet known. Further studies should attempt to obtain flux data along with concurrent spray data in order to fully understand the behavior of C_K and the role of sea spray at high winds.

References

Anderson, R. J., and S. D. Smith, 1981: Evaporation coefficient for the sea surface from eddy flux measurements. *J. Geophys. Res.,* **86**, 449-456.

Andreas, E. L, and K. A. Emanuel, 2001: Effects of sea spray on tropical cyclone intensity. *J. Atmos. Sci.,* **58,** 3741–3751.

Black, P. G., and Coauthors, 2006: In *Sixth WMO International Workshop on Tropical Cyclones*, WMO report TMPR 72, 214–255.

Blanc, T. V., 1985: Variation of bulk-derived surface flux, stability, and surface roughness results due to the use of different transfer coefficient schemes. *J. Phys. Oceanogr.,* **15**, 650–669.

Blanc, T. V., 1987: Accuracy of bulk-method-determined flux, stability, and sea surface roughness. *J. Geophys. Res.* **92**, 3867–3876.

Busch, N. E., 1972: On the mechanics of atmospheric turbulence. In *Workshop on Micrometeorology,* Boston, MA, Amer. Meteor. Soc. 1–65.

Businger, J. A., 1966: Transfer of momentum and heat in the planetary boundary layer. In *Proceedings of the Symposium on the Arctic Heat Budget and Atmospheric Circulation* (J.O. Fletcher, Ed.). Santa Monica, California: Rand Corporation, RM-52339NSF, 305–332.

Businger, J. A., J. C. Wyngaard, Y. Izumi, and E. F. Bradley, 1971: Flux-profile relationships in the atmospheric surface layer. *J. Atmos. Sci.,* **28**, 181–189.

Businger, J. A., 1973: Turbulent transfer in the atmospheric surface layer. In *Workshop on Micrometeorology* (D.A. Haugen, Ed.). Boston: Amer. Meteor. Soc., 67–100.

Businger, J.A., 1986: Evalustion of the accuracy with which dry deposition can be measured with current micrometeorological techniques. *J. Clim. Appl. Meteorol.,* **25**, 1100–1123.

Businger, J. A., 1988: A note on the Businger-Dyer profiles. *Bound.-Layer Meteor.,* **42**, 145–151.

Coppin, P. A., E. F. Bradley, I. J. Barton, and J. S. Godfrey, 1991: Simultaneous observations of sea surface temperature in the western equatorial Pacific Ocean by bulk, radiative and satellite methods, *J. Geophys. Res.,* **96**, 3401–3409.

DeCosmo, J., K. B. Katsaros, S. D. Smith, R. J. Anderson, W. A. Oost, K. Bumke, and H. Chadwick, 1996: Air–sea exchange of water vapor and sensible heat: The Humidity Exchange over the Sea (HEXOS) results. *J. Geophys. Res.,* **101,** 12001–12016.

Donelan, M. A., 1990: Air–sea interaction. *The Sea.* B. LeMéhauté and D. Hanes, Eds., Ocean Engineering Science, Vol. 9, John Wiley, 239–292.

Donelan, M. A., B. K. Haus, N. Reul, W. J. Plant, M. Stiassnie, H. C. Graber, O. B. Brown, and E. S. Saltzman, 2004: On the limiting aerodynamic roughness of the ocean in very strong winds. *Geophys. Res. Lett.,* **31,** L18306.

Drennan, W. M., J. Zhang, J. R. French, C. McCormick, and P. G. Black, 2007: Turbulent fluxes in the hurricane boundary layer. Part II: Latent heat flux. *J. Atmos. Sci.,* **64,** 1103–1115.

Dyer, A. J., and B. B. Hicks, 1970: Flux-gradient relationships in the constant flux layer. *Quarterly Journal of the Royal Meteorological Society,* **96**, 715–721.

Dyer, A. J., 1974: A review of flux-profile relationships. *Bound.-Layer Meteor.,* **7**, 363–372.

Dyer, A. J., and E. F. Bradley, 1982: An alternative analysis of flux-gradient relationships at the 1976 ITCE. *Bound.-Layer Meteor.,* **22**, 3–19.

Edson, J. B., C. W. Fairall, P. G. Mestayer, and S. E. Larsen, 1991: A study of the inertial-dissipation method for computing air-sea fluxes. *J. Geophys. Res.,* **96**, 10689–10711.

Emanuel, K. A., 1986: An air–sea interaction theory for tropical cyclones. Part I: Steady-state maintenance. *J. Atmos. Sci.,* **43,** 585–605.

Emanuel, K. A., 1995: Sensitivity of tropical cyclones to surface exchange coefficients and a revised steady-state model incorporating eye dynamics. *J. Atmos. Sci.,* **52,** 3969–3976.

Emanuel, K. A., 2003: A similarity hypothesis for air-sea exchange at extreme wind speeds. *J. Atmos. Sci.*, **60**, 1420-1428.

Emery, W. J., Y. Yu, G. A. Wick, P. Schluessel, and R. W. Reynolds, 1994: Correcting infrared satellite estimates of sea surface temperature for atmospheric water vapor attenuation, *J. Geophys. Res.,* **99**, 5219–5236.

Fairall, C. W., and S. E. Larsen, 1986: Inertial dissipation methods and turbulent fluxes at the air-ocean interface. *Bound.-Layer Meteor.,* **34**, 287–301.

Fairall, C. W., J. D. Kepert, and G. J. Holland, 1994: The effect of sea spray on surface energy transports over the ocean. *Global Atmos. Ocean Syst.,* **2,** 121–142.

Fairall, C. W., A. B. White, J. B. Edson, and J. E. Hare, 1997: Integrated shipboard measurements of the marine boundary layer. *J. Atmos. Oceanic Technol.,* **14,** 338–359.

Fairall, C. W., E. F. Bradley, J. E. Hare, A. A. Grachev, and J. B. Edson, 2003: Bulk parameterization of air–sea fluxes: Updates and verification for the COARE algorithm. *J. Climate,* **16,** 571–591.

French, J. R., W. M. Drennan, J. A. Zhang, and P. G. Black, 2007: Turbulent fluxes in the hurricane boundary layer. Part I: Momentum flux. *J. Atmos. Sci.,* **64,** 1089–1102.

Hasse, L., M. Grunewald, J. Wucknitz, M. Dunckel, and D. Schreiver, 1978: Profile derived turbulent fluxes in the surface layer under disturbed and undisturbed conditions during GATE. *Meteor. Forschungsergeb. Reihe B,* **13**, 24–40.

Hill, R. J., 1989: Implications of Monin-Obukhov similarity theory for scalar quantities. *J. Atmos. Sci.,* **46**, 2236–2244.

Högström, U., 1988: Non-dimensional wind and temperature profiles in the atmospheric surface layer: A re-evaluation. *Bound.-Layer Meteor.,* **43**, 55–78.

Hugen, D. A. (Ed.), 1973: *Workshop on Micrometeorology.* Boston: Amer. Meteor. Soc.

Large, W. G., and S. Pond, 1981: Open ocean momentum flux measurements in moderate to strong winds. *J. Phys. Oceanogr.,* **11,** 324–336.

Large, W. G., and S. Pond, 1982: Sensible and latent heat flux measurements over the ocean. *J. Phys. Oceanogr.,* **12,** 464–482.

Liu, W. T., K. B. Katsaros, and J. A. Businger, 1979: Bulk parameterization of the air–sea exchange of heat and water vapor including the molecular constraints at the interface. *J. Atmos. Sci.,* **36,** 2052–2062.

Makin, V. K., 1998: Air–sea exchange of heat in the presence of wind waves and spray. *J. Geophys. Res.,* **103,** 1137–1152.

Monin, A. S., and A. M. Obukhov, 1954: Basic laws of turbulent mixing in the ground layer of the atmosphere. *Trudy Inst. Theor. Geofiz., AN SSSR,* **24**, 163–187.

Montgomery, M. T., M. M. Bell, S. D. Aberson, and M. L. Black, 2006: Hurricane Isabel (2003): New insights into the physics of intense storms. Part I. Mean vortex structure and maximum intensity estimate. *Bull. Amer. Meteorol. Soc.,* **87**, 1335–1347.

Obukhov, A. M., 1946: Turbulence in thermally inhomogeneous atmosphere. *Trudy Inst. Theor. Geofiz., AN SSSR,* **1**, 95–115.

Ocampo-Torres, F. J., M. A. Donelan, N. Merzi, and F. Jia, 1994: Laboratory measurements of mass transfer of carbon dioxide and water vapour for smooth and rough flow conditions. *Tellus, Ser. B,* **46**, 16–32.

Panofsky, H. A., 1963: Determination of stress from wind and temperature measurements. *Quarterly Journal of the Royal Meteorological Society,* **89**, 85–94.

Panofsky, H. A., and J. A. Dutton, 1984: *Atmospheric Turbulence,* John Wiley, 397 pp.

Paulson, C. A., 1970: The mathematical representation of wind speed and temperature profiles in the unstable atmospheric surface layer. *Journal of Applied Meteorology,* **9**, 857–861.

Persing, J., and M. T. Montgomery, 2003: Hurricane superintensity. *J. Atmos. Sci.*, **60**, 2349–2371.

Plate, E. J., 1965; A research facility with concurrent air and water flows, *Houille Blanche,* **6**, 595.

Plate, E. J., 1978: Wind-generated water waves: The laboratory evidence, in *Turbulent fluxes Through the Sea Surface, Wave Dynamics and Prediction,* A. Favre and K. Hasselmann, Eds., Plenum, New York, 385–402.

Powell, M. D., P. J. Vickery, and T. A. Reinhold, 2003: Reduced drag coefficient for high wind speeds in tropical cyclones. *Nature,* **422,** 279–283.

Saunders, P. M., 1967: The temperature of the ocean-atmosphere interface, *J. Atmos. Sci.,* **24**, 269–273.

Schluessel, P., W. J. Emery, H. Grassl, and T. Mammen, 1990: On the bulk-skin temperature difference and its impact on satellite remote sensing of the sea surface temperature, *J. Geophys. Res.,* **95**, 13341–13356.

Smith, S. D., 1980: Wind stress and heat flux over the ocean in gale force winds. *J. Phys. Oceanogr.,* **10,** 709–726.

Smith, S. D., and R. J. Anderson, 1988: Bedford institute of oceanography eddy flux measurements during hexmax. In *Proceedings of the NATO Advanced Workshop: Humidity exchange over the sea: main experiment (HEXMAX), analysis and interpretation* (W. A. Oost, S. D. Smith, and K. B. Katsaros, Eds.). Dellenhove, Epe, The Netherlands, 14-21.

Smith, S. D., K. B. Katsaros, W. A. Oost, and P. G. Mestayer, 1990: Two major Experiments in the Humidity Exchange over the Sea Program. *Bull. Amer. Meteorol. Soc.,* **71**, 161-172.

Smith, S. D., and Coauthors, 1992: Sea surface wind stress and drag coefficients: The HEXOS results. *Bound.-Layer Meteor.,* **60,** 109–142.

Smith, S. D., C. W. Fairall, G. L. Geernaert, and L. Hasse, 1996: Air–sea fluxes: 25 years of progress. *Bound.-Layer Meteor.,* **78,** 247–290.

Webb, E. K., 1970: Profile relationships: The log-linear range and extension to strong stability. *Quarterly Journal of the Royal Meteorological Society,* **96**, 67–90.

Webb, E. K., G. I. Pearman, and R. Leuning, 1980: Correction of flux measurements for density effects due to heat and water vapour transfer. *Quarterly Journal of the Royal Meteorological Society,* **106,** 85–100.

Webster, P. J., and R. Lukas, 1992: TOGA COARE: The Coupled Ocean Atmosphere Response Experiment. *Bull. Amer. Meteorol. Soc.*, **73**, 1377-1416.

Wieringa, J., 1980: A revaluation of the Kansas mast influence on measurements of stress and cup anemometer overspeeding. *Bound.-Layer Meteor.,* **18**, 411–430.

Woodcock, A. H., 1941: Surface cooling and streaming in shallow, fresh, and salt water, *J. Mar. Res.,* **4**, 153–161.

Wu, J., 1979: Oceanic whitecaps and sea state. *J. Phys. Oceanogr.,* **9,** 1064–1068.

Wu, J., 1980: Wind-stress coefficients over sea surface near neutral conditions - A revisit. *J. Phys. Oceanogr.*, **10**, 727-740.

Wu, J., 1992: On moisture flux across the Sea Surface. *Bound.-Layer Meteor.,* **60**,361-374.

Wyngaard, J. C., 1973: On surface-layer turbulence. In *Workshop on Micrometeorology* (D.A. Haugen, Ed.). Boston: Amer. Meteor. Soc., 101–149.

Wyngaard, J. C., 1990: Scalar fluxes in the planetary boundary layer: Theory, modeling, and measurement, *Bound.-Layer Meteor.,* **50**, 49–75.

Zhang, J., 2007: *An airborne investigation of the atmospheric boundary layer structure in the hurricane force wind regime.* Ph.D. thesis, University of Miami, Miami, 149 pp.

Zhang, J. A., P. G. Black, J. R. French, and W. M. Drennan, 2008: The first direct measurements of enthalpy flux in the hurricane boundary layer: the CBLAST results. *Geophys. Res. Lett.*, in press.

Zilitinkevich, S. S., 1966: Effect of humidity stratification on hydrostatic stability. *Akademiia Nauk SSSR, Atmospheric and Oceanic Physics,* **2**, 655–658.